LUND UNIVERSITY
Faculty of Science

Combining the GW Approximation with the Hubbard I Approximation for strongly correlated materials

Torsten Strunck

Thesis submitted for the degree of Master of Science
Project duration: 4 months

Supervised by Prof. Ferdi Aryasetiawan
Co-supervised by Dr. Fredrik Nilsson

Department of Physics
Division of Mathematical Physics
June 2019

1 Abstract

In this thesis, the GW approximation (GWA, Green's function G times screened interaction W) and the Hubbard I approximation (HIA) are combined in a non-self-consistent one-shot calculation to determine the electronic structure of a one-dimensional strongly-correlated model. The scheme was chosen to incorporate both screening effects through the GWA and strong on-site correlations through the atomic HIA. The resulting self-energies of both methods are summed together and another term is subtracted to correct double-counting. The examined double-counting terms were the local self-energy of the GWA result, the GWA self-energy of the atomic model used in the HIA and lastly the impurity self-energy within the GWA. The self-energy of the atomic model in the HIA was solved analytically. It was found that all three approaches yield non-causal features, which increase with the on-site Coulomb repulsion, in the resulting spectral function. The local GWA self-energy was observed to perform best in terms of causality and computational effort. Changes in the resulting quasi-particle structure in the spectral function showed that screening effects and local correlations were included successfully.

Contents

Abbreviations

GF	Green's function
GWA	GW Approximation
HIA	Hubbard I Approximation
DMFT	Dynamical Mean Field Theory
AIM	Anderson impurity model
PES	Photoemission Spectrum
IPES	Inverse Photoemission Spectrum
DFT	Density Functional Theory
HFA	Hartree-Fock approximation

Acknowledgements

I would like to thank Ferdi Aryasetiawan for having granted me this opportunity and guiding me through the project. His patience and helpfulness were incredibly valuable and inspiring to me.

I also thank Fredrik Nilsson who was just as helpful and contributed ideas and corrections to the project and thesis.

Special thanks go to Tor Sjöstrand who happily discussed the analytic solution with me.

I would like to thank my parents Volker and Birgit and my sister Marion for always supporting me in what I do and also proofreading my thesis.

Furthermore, I am inexpressibly thankful for Ariane for always being there for me and supporting me in my life.

2 Introduction

The electronic structure of solids is of high interest in physics, as it provides important information about the properties of a material such as its optical characteristics, conductivity, susceptibility, etc. This knowledge is utilized in many ways to understand the mechanisms behind these properties and to design materials for many applications, e.g., lasers or solar panels.

Since a solid contains a large number of interacting particles, the exact determination of its electronic structure for large systems is impossible with our current means of computation. The problem can be made clear by taking a look at the Hamiltonian of a solid

$$H = \sum_i^N \left[-\frac{1}{2}\nabla^2(r_i) + V(r_i) \right] + \underbrace{\frac{1}{2}\sum_{i \neq j}^N \frac{1}{|r_i - r_j|}}_{\text{Coulomb interaction}} \tag{1}$$

for which the Schrödinger equation has to be solved:

$$i\frac{\partial}{\partial t}\left|\Psi(t)\right\rangle = H\left|\Psi(t)\right\rangle \ . \tag{2}$$

This Hamiltonian describes electron correlations in a solid, whereas interactions including nuclei have already been reduced to an external potential V. Relativistic effects have been dropped, too. This leaves three terms, where the first term represents the electrons' kinetic energy and the second term the coupling to atoms. The sum goes over all N electrons in the solid with r_i being the position of electron i. The last term is the reason why it is so hard to solve this problem exactly: It is a non-local term which couples each electron to all other electrons. This makes it difficult to solve for systems with large N like solids or already remotely large molecules. Nevertheless, many properties can be reasonably approximated through the usage of mathematical and numerical methods which simplify this non-local many-body problem, and it is still of current interest to improve these methods and find new ones.

To circumvent this problem, approximations for the Coulomb term are needed. In the history of solid state theory several models were established and improved upon. One of the earliest is the *Hartree Approximation* (1928) in which the term is substituted by an average local potential. The *Hartree-Fock method* (1930) expanded this through the inclusion of the fermionic nature of electrons. Yet, this approximation did not include screening and correlation effects of electrons in the system. Therefore, the band gaps of insulators were often overestimated, as the neglected effects result in a reduction of the Coulomb energy.

With the introduction of the Hohenberg-Kohn theorems [9] the *Density Functional Theory* (DFT) was moved into the spotlight. The theorems prove that the electron density uniquely determines the ground- and excited-state properties of a many-electron system and define an energy functional which is minimized by the correct ground-state electron density. Assuming a system of non-interacting particles resulting in the same density as the system of interacting particles, the Kohn-Sham equations are defined as

$$\left(-\frac{1}{2}\nabla^2 + V_H + V_{xc} + V_{ext} \right) \phi_i = \epsilon_i \phi_i \ . \tag{3}$$

V_H here is the Hartree potential, V_{xc} the exchange-correlation potential and V_{ext} the external potential. $V_{KS} = V_H + V_{xc} + V_{ext}$ is also referred to as the Kohn-Sham potential. The eigenvalues of this equation ϵ_i are often interpreted as single-particle excitation energies although a theoretical justification for this has only been found for the energy of the highest occupied state [14]. The Kohn-Sham potential is usually approximated through the *Local Density Approximation* (LDA) where the density is replaced by a local density (derived from the homogeneous electron gas model).

The LDA provides reasonable results for the ground-state properties of materials and despite the missing theoretical justification, the eigenvalues of the Kohn-Sham equation mostly describe the excitation energies correctly. Yet, there are a number of properties where the LDA yields imprecise results, e.g., for the band gaps of semiconductors and the spectral function of d- and f-systems.

Alternatively to DFT, a proper approach was the Green function theory which grants a theoretically justified equation for the determination of the single-particle excitation energies E_i according the quasi-particle equation

$$\left(-\frac{1}{2}\nabla^2(r) + V_H(r)\right)\Psi_i(r) + \int d^3r'\Sigma(r,r';E_i)\Psi_i(r') = E_i\Psi_i(r) \ . \tag{4}$$

Σ equals the self-energy which contains the exchange correlation effects. To determine this self-energy term became the new difficulty. The self-energy can be approximated with the *GW approximation* [8] where a perturbative expansion of Σ in terms of the single-particle Green's Function G and the screened Coulomb interaction W is truncated after the first term. Schematically this can depicted be as:

$$\Sigma = iGW - GWGWG + ... \quad \Rightarrow \quad \Sigma \approx iGW \ . \tag{5}$$

This approximation was found to be feasible for many materials, providing better results for most of the band gaps which were underestimated by the LDA, as can be seen in Fig. (2), as well as granting more precise single-particle excitation energy dispersions.

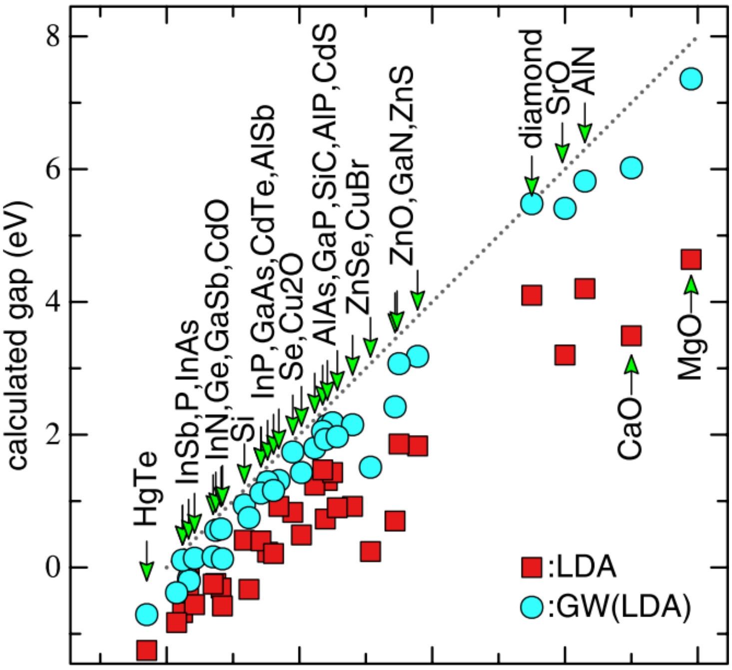

Figure 2: Comparison of the band gap estimations between the GWA and LDA for several materials. The figure is taken from [24].

Yet, strongly correlated materials like transition metal compounds or Mott insulators yield discrepancies when this method is applied to them.

Strongly correlated materials are characterized by very localized orbitals with little overlap like the 3d- or 4f-systems and have partially filled and very narrow bands. This gives rise to strong Coulomb repulsion between electrons occupying these orbitals. To explore electron correlations in narrow energy bands, the Hubbard model was constructed [10], focusing on the interaction of electrons on the same atomic site. Solving this model exactly was found to be difficult, yet approximations were formulated to overcome this problem. One approximation for this is the Hubbard I approximation (HIA) [10] which simplifies the many-body non-local problem to a local atomic model. An improvement over this is the Dynamical Mean Field Theory (DMFT) which maps onto a self-consistent local many-body problem, an "impurity model".

The aim of this project was to use the GW approximation, to account for long-range interactions, and combine it with the Hubbard I approximation for short-range correlations which effectively solves the multiplet problem. By including the GWA, screening effects will also be taken into account which can have a decisive influence on strongly-correlated materials [3]. The results should give insight into the band structure of these materials while being less computationally expensive than full DMFT calculations. A similar approach has already been implemented as LDA+HIA [16], yielding reasonable results but it also has a problem with double-counting due to interaction terms both in LDA and Hubbard I, which can be managed in GW+HIA. Another recent advance in this field has been the implementation of GW + extended DMFT [19]. Many strongly correlated materials have already been discovered and are being synthesized up to date for applications like magnets, lasers and high-temperature superconductors whose theoretical mechanisms are still being investigated to this day.

This report is split into four parts. The first part Sec. (3) gives information about the theoretical background by summarizing physical phenomena and mathematical methods. In the next section Sec. (4), the methods which have been used in this project and their application are elucidated. Results and their interpretation are presented in Sec. (5). Lastly, an outlook including potential improvements is given.

3 Theoretical Background

3.1 Photoemission Spectroscopy and quasi-particles

A common method to study the electronic structure of strongly correlated materials is photoemission spectroscopy (PES). The sample is probed by light of a tunable wavelength to measure the response of the system. Photons with enough energy will excite electrons through interaction out of the material. This phenomenon is called the photoelectric effect. By measuring the kinetic energy of the emitted photoelectrons, conclusions about the (former) occupied states can be made through the following equation:

$$E_{kin} = E_\gamma - E_B - \Phi_0 \; . \tag{6}$$

Due to conservation of energy, the kinetic energy E_{kin} of the emitted electron is equal to the incoming photon's energy E_γ, minus the electron's prior binding energy E_B and work function Φ_0, which is the energy needed to take the electron into the vacuum. Thus, the binding energy can be determined. A scheme and typical measurement graph are presented in Fig. (3) below.

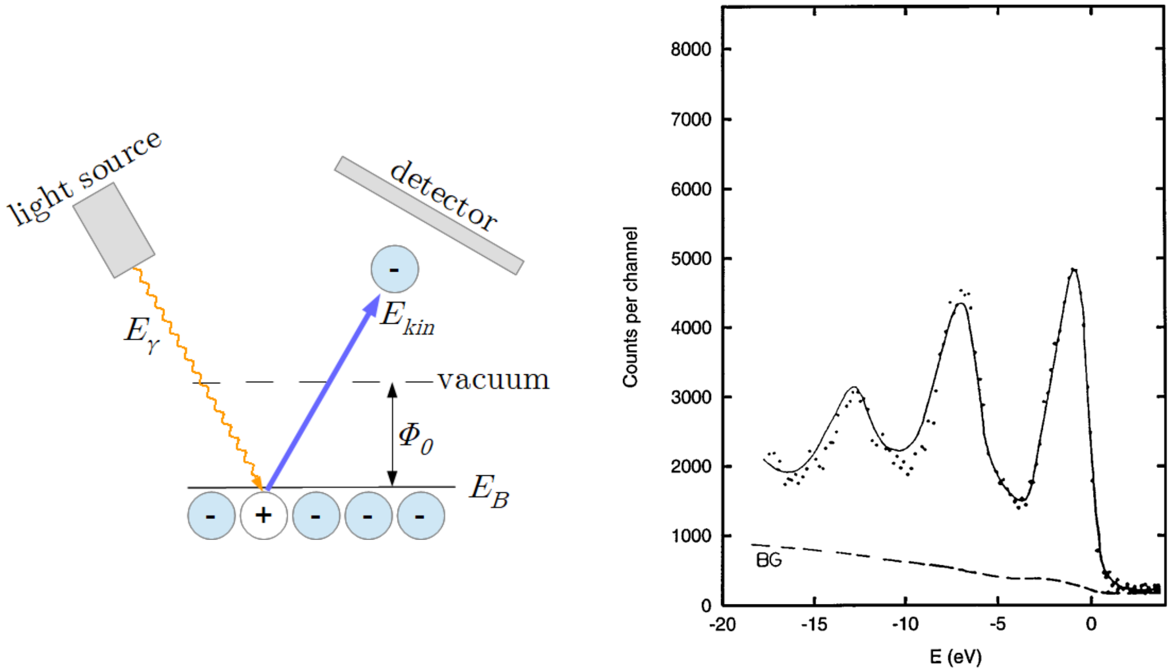

Figure 3: A scheme of the PES process (left) and a spectrum measurement of Na (right). The spectrum plot is taken from [2], in which the dots are experimental data, while the solid line is a convolution of computational and experimental data. The dashed line "BG" is the estimated background contribution.

Related methods are inverse PES (IPES), where an electron beam is used to probe and analyze unoccupied states, as well as angle-resolved photoemission spectroscopy (ARPES) which refines PES by also measuring the electrons' momenta.

One important notion about photoemission is the screening effect, following a removal of an electron. As the electron is emitted from the material, the leftover site can be seen as a positively charged hole in the lattice which attracts surrounding electrons, which in turn screen this hole from interactions with other electrons. Thus, the hole and the surrounding screening electrons become a quasi-particle, which interacts based on the screened Coulomb potential W instead of the bare Coulomb potential. The process is depicted schematically in Fig (4).

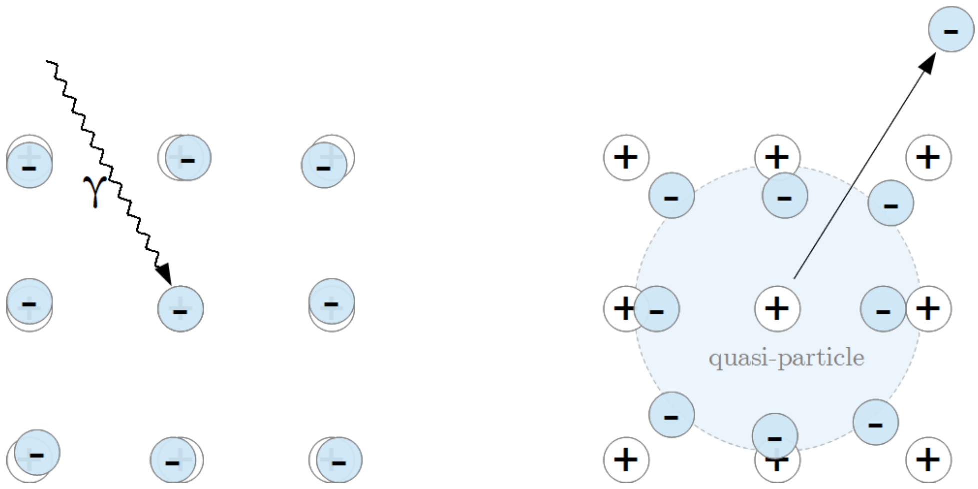

Figure 4: A photoemission experiment in which the lattice is probed with a photon (left) and emits an electron, followed by a screening effect of the surrounding electrons (right).

Another type of quasi-particles is the plasmon, which is the quantized description of electron density oscillations. Scattering of plasmons with other particles is an important factor for the properties of materials. For instance, if a perturbation has a frequency higher than the plasmon frequency, then the electrons cannot respond quickly enough to screen the perturbation. The excitations of plasmons are given by the poles of the inverse dielectric function $1/\epsilon(k,\omega)$ which is proportional to the screened Coulomb potential $W(k,\omega)$.

3.2 Green's function theory

A mathematical way to describe the processes happening during PES is through Green's function theory. The mathematical Green's function can be understood as the response to an infinitesimal probe, by which the response to any other probe can be derived. In many-body theory, the single-particle Green's function for electrons is defined as follows:

$$\begin{aligned} G(1,2) &= -i\left\langle \Psi_0^{(N)} \middle| T(\hat{\psi}(1)\hat{\psi}^\dagger(2)) \middle| \Psi_0^{(N)} \right\rangle \\ &= \begin{cases} -i\left\langle \Psi_0^{(N)} \middle| \hat{\psi}(1)\hat{\psi}^\dagger(2) \middle| \Psi_0^{(N)} \right\rangle, \text{ for } t_1 > t_2 \text{ (electron)} \\ +i\left\langle \Psi_0^{(N)} \middle| \hat{\psi}(2)\hat{\psi}^\dagger(1) \middle| \Psi_0^{(N)} \right\rangle, \text{ for } t_1 < t_2 \text{ (hole)} \end{cases} . \end{aligned} \tag{7}$$

Argument 1 (and 2) are to be understood as representing the variables position $\boldsymbol{r}_1$, spin σ_1 and time t_1. The bra and ket states $\left|\Psi_0^{(N)}\right\rangle$ express the N-particle ground-state. The time-ordering operator T sorts the target operators timewise, with the latest time argument to the left, taking commutation rules into consideration. $\hat{\psi}^\dagger(1)$ is a quantum-field operator in the Heisenberg picture, which creates an electron at position r_1 with spin σ_1 and at time t_1. Correspondingly, $\hat{\psi}(1)$ destroys an electron at 1. The Green's function can be understood as the probability amplitude of an electron that is added at position 2 to propagate to position 1 if $t_1 > t_2$, or analogously for $t_1 < t_2$ a hole that is created at position 1 to propagate to position 2. By knowing the Green's function of a system, many properties can be determined, e.g., the excitation spectrum, the ground state energy or the expectation value of any one-particle operator in the ground state [1].

The structure of G can be made clearer by rewriting it in the Lehmann representation:

$$G(r_1, r_2; \omega) = \sum_n \frac{g_n(r_1) g_n^*(r_2)}{\omega - (E_n^{N+1} - E_0^N) + i\delta} + \sum_n \frac{f_n(r_1) f_n^*(r_2)}{\omega - (E_n^{N-1} - E_0^N) - i\delta} \ . \tag{8}$$

E_n^N is the eigenenergy of the state $\left|\Psi_n^N\right\rangle$. Here the quasi-particle amplitudes were introduced:

$$g_n(r) = \left\langle \Psi_0^{(N)} \right| \hat{\psi}(r) \left| \Psi_n^{(N+1)} \right\rangle \qquad \text{and} \qquad f_n(r) = \left\langle \Psi_n^{(N-1)} \right| \hat{\psi}(r) \left| \Psi_0^{(N)} \right\rangle \ . \tag{9}$$

This shows that the Green's function has poles at the energy differences between the groundstate energy and the energy of the $N \pm 1$ eigenstates, with amplitudes depending on the quasi-particle amplitudes. The first sum treats quasi-particle excitations caused by the addition of an electron $(N + 1)$ while the second sum represents the addition of a hole $(N - 1)$. In a single-particle picture one can think of the addition of an electron as the probing of unoccupied states and thus the IPES spectrum, while the removal of an electron represents the PES spectrum and the probing of occupied states. The pole structure can be made clearer by using the approximation $E_0^{(N+1)} - E_0^N \approx \frac{dE_0}{dN}\big|_N = \mu(N) \approx \mu(N-1) \equiv \mu$ for large N with the chemical potential μ and rewriting the denominators in the following way:

$$\begin{aligned} \omega - (E_n^{(N+1)} - E_0^{(N)}) + i\delta &= \omega - (E_n^{(N+1)} - E_0^{(N+1)}) - (E_0^{(N+1)} - E_0^{(N)}) + i\delta \\ &\approx \omega - (E_n^{(N+1)} - E_0^{(N+1)}) - \mu + i\delta \ , \\ \omega + (E_n^{(N-1)} - E_0^{(N)}) - i\delta &\approx \omega + (E_n^{(N-1)} - E_0^{(N-1)}) - \mu - i\delta \ . \end{aligned}$$

Thus, the poles are aligned around μ and can be schematized as in Fig. (5) below.

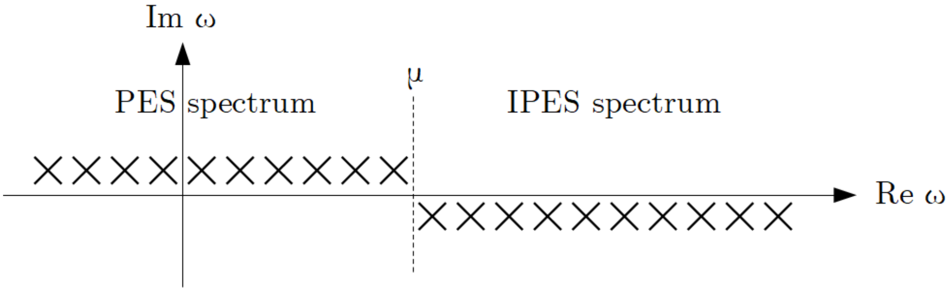

Figure 5: The pole structure of the Green's function $G(\omega)$.

The trace of the spectral function A of the Green's function

$$A(r, r'; \omega) = -\frac{1}{\pi} sgn(\omega - \mu) \, \mathrm{Im} \, G(r, r'; \omega) \tag{10}$$

can be interpreted as the density of states observed in experiments. The spectral function has the same pole structure as G but is positive definite because of the sign function. If it is negative for a certain frequency ω, causality is violated, i.e., the Green's function would have a non-zero amplitude for the particle before it is created, or after it is destroyed. The Green's function can be written in terms of its spectral function as:

$$G(r, r'; \omega) = \int_{-\infty}^{\mu} d\omega' \frac{A(r, r'; \omega')}{\omega - \omega' - i\delta} + \int_{\mu}^{\infty} d\omega' \frac{A(r, r'; \omega')}{\omega - \omega' + i\delta} \ . \tag{11}$$

The PES/IPES or occupied/unoccupied structure is again visible through the integrals to and from μ. In the non-interacting case, where there is no broadening due to excitations like plasmons, the spectral function is a series of delta functions:

$$A_0(r, r'; \omega) = \sum_n \psi_n(r)\psi_n^*(r')\delta(\omega - \epsilon_n) \ . \tag{12}$$

The non-interacting Green's function can then be written as

$$G^0(r, r'; \omega) = \sum_n^{occ} \frac{\psi_n(r)\psi_n^*(r')}{\omega - \epsilon_n - i\delta} + \sum_n^{unocc} \frac{\psi_n(r)\psi_n^*(r')}{\omega - \epsilon_n + i\delta} \ , \tag{13}$$

where $i\delta$ is an infinitesimal quantity and the two sums go over occupied and unoccupied bands n respectively with the corresponding eigenenergies ϵ_n and eigenstates $\psi_n(r)$.

3.3 The self-energy

The potential a particle experiences through the changes it causes itself in its environment is called the self-energy Σ. An example of such an effect is the screening as described in Sec. (3.1). The self-energy is generally non-local and energy-dependent, as interactions with the surroundings are influenced by the energy or state the particle itself occupies. It is described through the quasi-particle equation:

$$\left[-\frac{1}{2}\nabla^2 + V_H(r)\right]\Psi_k(r) + \int d^3r'\Sigma(r, r'; E_k)\Psi_k(r') = E_k\Psi_k(r) \ , \tag{14}$$

where $V_H(r)$ is the Hartree potential and E_k and Ψ_k are the quasi-particle energies and eigenstates, respectively. Possible quantities which can be deduced from the self-energy, corresponding to the spectral function as depicted in Fig. (6), are the following:

– Quasi-particle band structure:

$$E_{nk} = \epsilon_{nk} + \mathrm{Re}(\Sigma(k, E_{nk})) \tag{15}$$

– Spectral weight:

$$Z_{nk} = \left(1 - \frac{\partial\,\mathrm{Re}(\Sigma(k,\omega))}{\partial\omega}\right)^{-1}\Bigg|_{w=E_{nk}}$$

– Quasi-particle lifetime:

$$\tau_{nk}^{-1} \propto \Gamma_{nk} = \mathrm{Im}(\Sigma(k, E_{nk})) \tag{16}$$

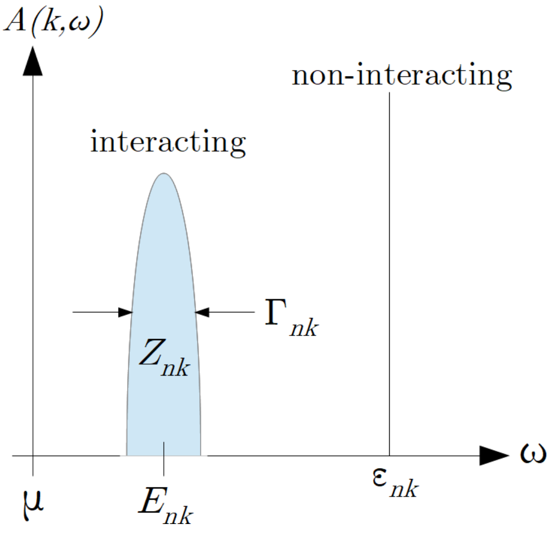

Figure 6: Scheme of the spectral function.

As the non-interacting spectral function is a series delta functions, a non-interacting particle has exactly the energy ϵ_{nk}. By including many-body interactions, the spectral weight is spread out, through the many-body self-energy. Assuming that the self-energy is diagonal in the band index n, the interacting spectral function can be written in terms of the self-energy as:

$$A(k,\omega) = \sum_n \frac{\mathrm{Im}(\Sigma_n(k,\omega))}{(\omega - \epsilon_n(k) - \mathrm{Re}(\Sigma_n(k,\omega))^2 + \mathrm{Im}(\Sigma_n(k,\omega))^2)} \ . \tag{17}$$

Through the equation of motion of the field operators one can derive the Dyson equation which is schematically written as

$$G = G_0 + G_0 \Sigma G \ . \tag{18}$$

3.4 The Hedin equations and the GW-Approximation

In 1965 Lars Hedin [8] introduced a complete set of equations, which describe the self-energy in terms of the screened Coulomb interaction W. These so-called Hedin equations, shown in Eqs. (19 to 23), are self-consistent and exact:

$$\text{self-energy} \qquad \Sigma(1,2) = i \int d(34) G(1,3^+) W(1,4) \Lambda(3,2,4) \ , \tag{19}$$

$$\text{Green's function} \qquad G(1,2) = G_0(1,2) + \int d(34) G_0(1,3) \Sigma(3,4) G(4,2) \ , \tag{20}$$

$$\begin{aligned} \text{vertex function} \qquad \Lambda(1,2,3) &= \delta(1-2)\delta(2-3) \\ &+ \int d(4567) \frac{\Sigma(1,2)}{G(4,5)} G(4,6) G(7,5) \Lambda(6,7,3) \ , \end{aligned} \tag{21}$$

$$\text{polarization} \qquad P(1,2) = -i \int d(34) G(1,3) \Lambda(3,4,2) G(4,1^+) \ , \tag{22}$$

$$\text{screened interaction} \qquad W(1,2) = v(1,2) + \int d(34) v(1,3) P(3,4) W(4,2) \ . \tag{23}$$

Here, $v(1,2)$ is the bare Coulomb interaction. To solve this set of equations exactly for real systems is impossible. An approximation is usually used to determine an initial result for Σ. Through iterative calculations higher order results can then be achieved. Hedin proposed therefore to truncate higher orders of the vertex function, as displayed in the following equation:

$$\Lambda(1,2,3) \approx \delta(1-2)\delta(2-3) \ . \tag{24}$$

This results in the so-called **GW Approximation** (GWA). Again, higher order results can be determined through iterative calculations.

GW Approximation

$$\Sigma \approx iGW \tag{25}$$

A scheme of the Hedin equations and the GWA is presented in Fig. (7) below.

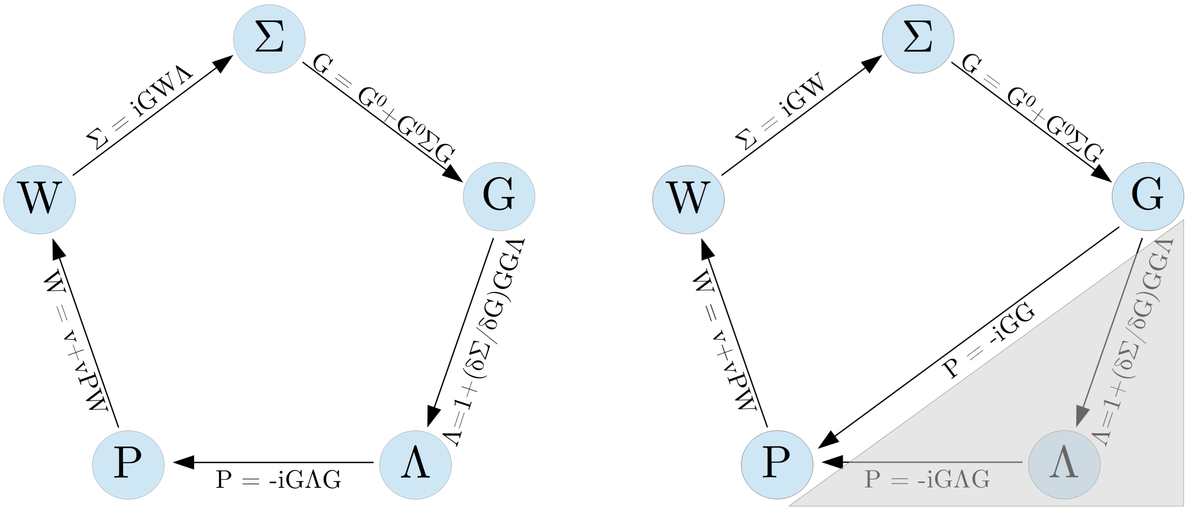

Figure 7: Scheme of the Hedin equations or "Hedin's wheel" (recreated from [6]). The left figure shows the exact equation set, whereas the GW approximation is depicted in the right figure with the vertex function set to identity.

3.5 Strongly correlated materials

d- or f-shells in materials give raise to very narrow bands, which have great influence on their properties, especially if they are partially filled. Electrons which occupy these shells are very localized around the nucleus making it possible to refer to them being *on* a specific atom [10]. Due to the small average distance between these electrons, strong Coulomb repulsion dominates their interactions and thus reduces the likelihood for two electrons to occupy the same orbital. This is why these materials are called *strongly correlated*.

Mean-field theories like Hartree-Fock, which generally assume non-interacting electrons, thus break down for strongly correlated materials, as the electron-electron correlations play an important role.

An example of this type of materials are the so-called Mott insulators like NiO, which has a partially filled 3d shell. Traditional band theory predicts this material to behave conducting, but it is an insulator due to electron correlations [18]. Other interesting properties are Mott metal-insulator transitions [12], high temperature superconductivity [26] and colossal magnetoresistance [29]. To describe these materials, improvements and new models have been designed. A simple model to describe strong "on-site" correlations is the Hubbard model, which will be introduced in Sec. (3.6) along with Dynamical Mean Field Theory (DMFT).

3.6 The Hubbard model

The **Hubbard model** was constructed in the 1960s to qualitatively describe strongly correlated materials, specifically $3d$ transition metals [10]. It is assumed that the strong correlations dominate the properties of these materials, so that other bands are neglected. A fixed lattice of sites is examined, where each site contains one s-like orbital, i.e. with two occupying electrons at most. Furthermore, electrons may hop between the sites, and only on-site interactions are considered for correlation effects. The Hamiltonian of the one-band, spin-1/2 Hubbard model is depicted below:

$$H^{Hubbard} = \sum_{\langle ij\rangle\sigma} t_{ij}\hat{c}^{\dagger}_{i\sigma}\hat{c}_{j\sigma} + U\sum_{i}\hat{n}_{i\uparrow}\hat{n}_{i\downarrow}\ . \tag{26}$$

The first term describes the kinetic aspect where electrons are enabled to hop from lattice site j to i depending on a hopping parameter t_{ij}. The sum only ranges over spins σ and nearest neighbors, denoted by $\langle ij\rangle$. $\hat{c}^{\dagger}_{i\sigma}$ is the fermionic creation operator at site i and spin σ, $\hat{c}_{i\sigma}$ the annihilation operator. This term is based upon the tight-binding model. The hopping term arises from overlapping orbitals in solids. The second term describes the Coulomb forces of electrons on the same site where the energy increases for each such correlation by a parameter U. This parameter takes into account short-range interactions. $\hat{n}_{i\sigma} = \hat{c}^{\dagger}_{i\sigma}\hat{c}_{i\sigma}$ is the number operator. Thus, this model is good for systems with strong on-site correlations. The Hubbard model predicts the Mott metal-insulator transition [7] [22] through the variation of the two parameters t and U. The two terms in the Hamiltonian compete with each other in magnitude and describe a phase transition from an insulator for large values of U/t, which suppresses the propagation of electrons in the material, to a metal with a small U/t ratio, where electrons hop freely. Interestingly, it was found that the one-dimensional half-filled Hubbard model has an absence of this transition [15]. Thus, no such transition should appear for the model treated in this project either. Analytic solutions for this model have only been found for one dimension [15] or infinite dimensions [17] so far. Other dimensions have proven to be more difficult to solve and thus are usually examined through approximations and numerical methods [27] [11] [23]. Since the occupation of the lattice sites changes over time in this model, approximations must be dynamical. High Coloumb repulsion U suppresses double occupations, which means $\langle\hat{n}_{i\uparrow}\hat{n}_{i\downarrow}\rangle \neq \langle\hat{n}_{i\uparrow}\rangle\langle\hat{n}_{i\downarrow}\rangle$. As a consequence, this makes approximations in which the interaction term is factorized, like the Hartree-Fock method, unsuitable for strongly correlated materials.

3.7 DMFT and the Hubbard I Approximation

Dynamical Mean Field Theory (DMFT) is an approximate description of the electronic structure for strongly correlated many-body systems in a lattice (for further reading, see e.g. [28] and [21]). The initial many-body lattice problem is essentially mapped onto a many-body local problem, a so-called **impurity model**, as depicted in Fig. (8) below.

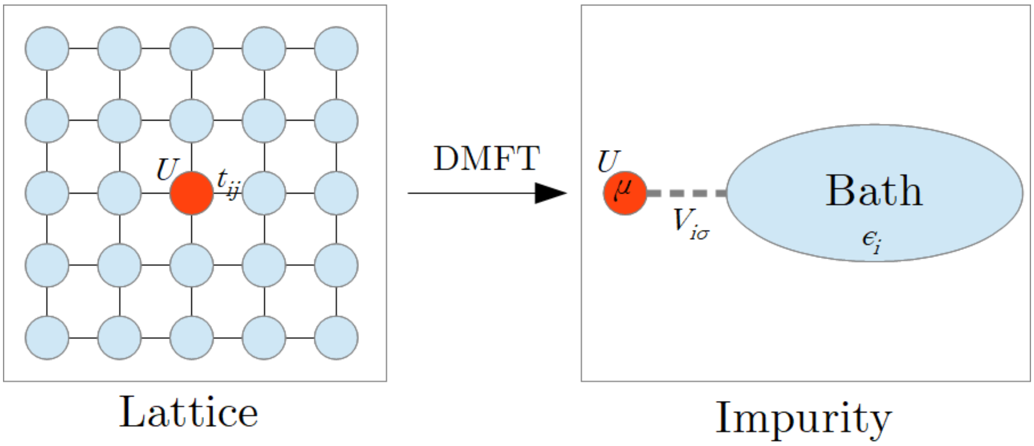

Figure 8: DMFT schematic. The lattice model is mapped to an impurity problem.

Instead of considering the whole lattice, a bath of non-correlated electronic levels is introduced and coupled to a single site. Thus, strong on-site interactions are preserved, while interaction with other sites is approximated through an effective mean-field, the bath. The self-consistently determined hybridization function $\Delta(t)$, which governs the coupling between the bath and the site, i.e. the electrons hopping in and out of the bath, is time dependent and thus makes the theory dynamical. It is defined as

$$\Delta(\omega) = \sum_{i\sigma} \frac{|V_{i\sigma}|^2}{\omega - \epsilon_i} \tag{27}$$

via the coupling parameter $V_{i\sigma}$ with which the impurity Green's function is then determined:

$$G^{imp}(\omega) = \frac{1}{\omega + \mu - \Delta(\omega) - \Sigma^{imp}(\omega)} \; . \tag{28}$$

Now, it is assumed that lattice self-energy is equal to the local self-energy of the impurity model

$$\Sigma^{lat}(\boldsymbol{k}, \omega) \approx \Sigma^{imp}(\omega) \; , \tag{29}$$

i.e. spatial fluctuations of the self-energy are neglected. Therefore the following self-consistency condition is imposed on the observable:

$$\text{self-consistency condition} \qquad G^{imp} \overset{!}{=} G^{loc} \tag{30}$$

with

$$G^{loc}(\omega) \approx \sum_{k} \frac{1}{\omega + \mu - \epsilon(k) - \Sigma^{imp}(\omega)} \; . \tag{31}$$

The reasoning behind DMFT is that in the limit of infinite dimensions, meaning that every site has an infinite number of neighbors, the approximation becomes exact [17]. A scheme of the self-consistent DMFT computation routine is depicted in Fig. (9).

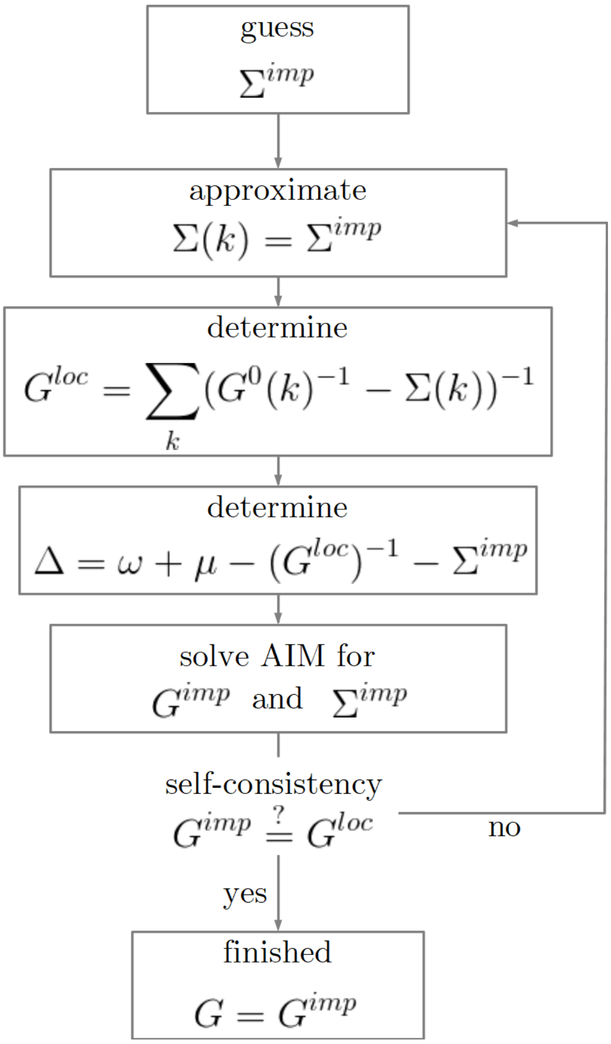

Figure 9: Scheme of the DMFT loop.

3.7.1 Anderson impurity model

To solve the Hubbard model via DMFT, it is mapped to the **Anderson impurity model** (AIM). The lattice is reduced to a bath of non-correlated electronic levels, coupled to a single site. The Hamiltonian is as follows:

$$H^{AIM} = \underbrace{\sum_{i\sigma} \epsilon_i \hat{a}^\dagger_{i\sigma} \hat{a}_{i\sigma}}_{bath} + \underbrace{\sum_{i\sigma} \left(V_{i\sigma} \hat{a}^\dagger_{i\sigma} \hat{c}_\sigma + h.c. \right)}_{coupling} + \underbrace{U \hat{n}_\uparrow \hat{n}_\downarrow - \mu(\hat{n}_\uparrow + \hat{n}_\downarrow)}_{impurity} \ . \tag{32}$$

The first term describes the electronic levels ϵ_i of the bath, where $\hat{a}^\dagger_i$ and $\hat{a}_i$ represent the creation and annihilation operators, respectively. The coupling between bath and impurity is determined by the second term with hybridization parameters $V_{i\sigma}$. The last two terms describe the single site impurity through the on-site Coulomb interaction and lastly the site's potential μ.

3.7.2 Hubbard I Approximation

DMFT not only becomes exact for infinite dimensions, but also in the limit of zero hopping. Zero hopping essentially decouples the bath from the single site, due to which only the single site by itself may be examined, resulting simply in an atomic problem. In the **Hubbard I Approximation**, the initial lattice problem is mapped onto an atomic problem [10]. This approximation is thus only reasonable for materials in which on-site correlations dominate. The approximation is then the following:

Hubbard I Approximation

$$\Sigma^{lat}(\boldsymbol{k},\omega) \approx \Sigma^{at}(\omega) \tag{33}$$

A scheme of the mapping is depicted in Fig. (10) below.

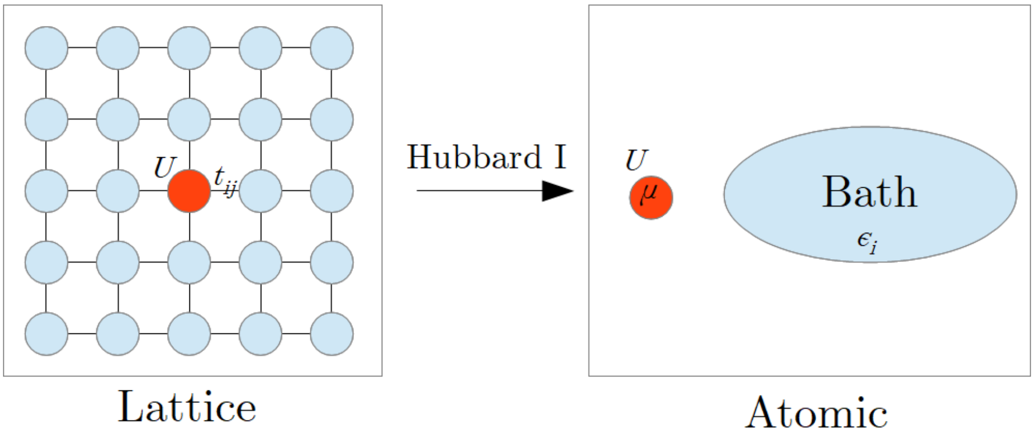

Figure 10: The Hubbard I Approximation maps a lattice problem to an atomic model.

4 Methodology

The general procedure is schematized in Fig. 11 below.

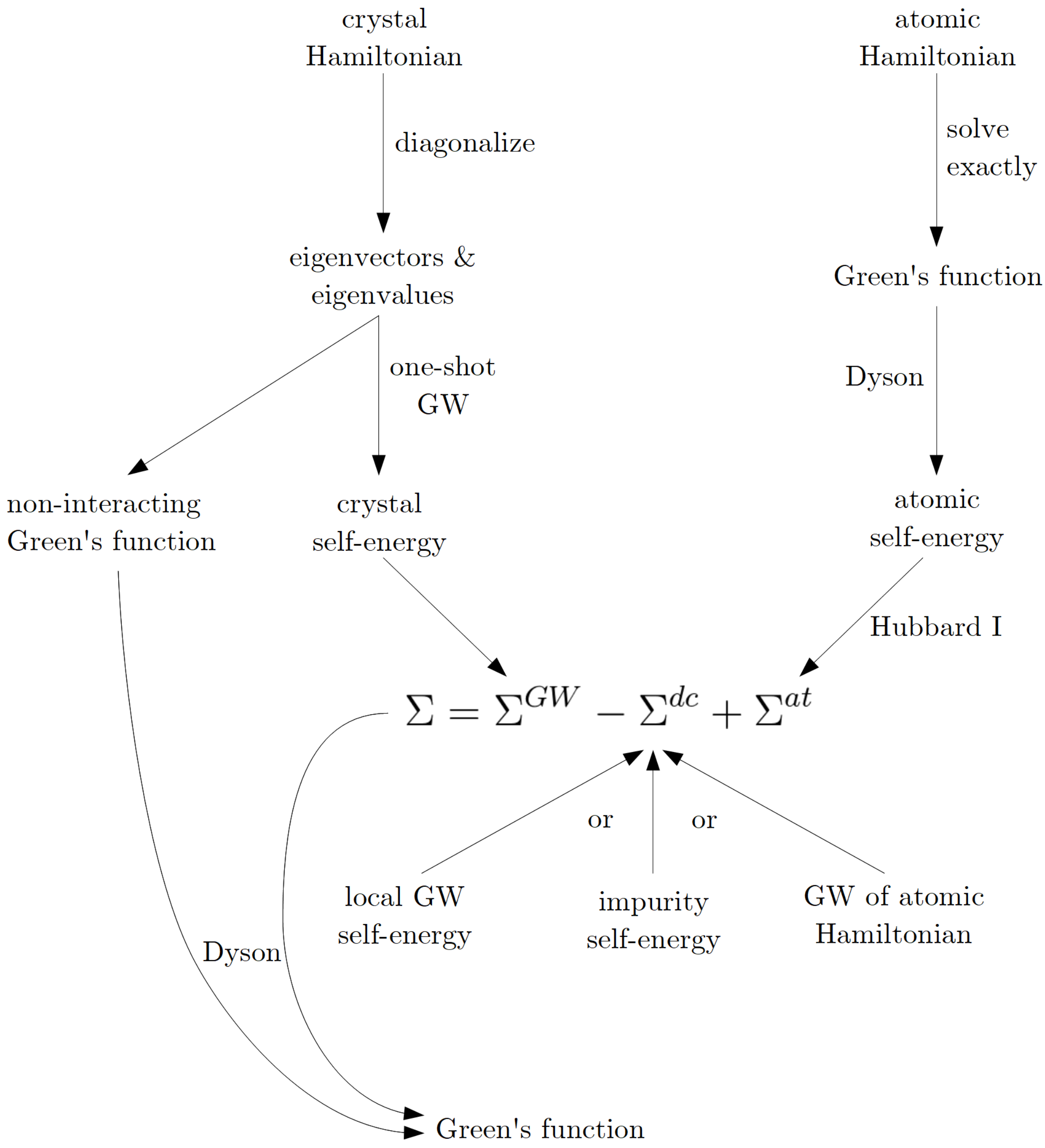

Figure 11: Procedure scheme of GWA+HIA with corrections for double-counting.

4.1 GW preparation

For testing the GWA+HIA scheme, a one-dimensional unit cell with periodic boundary conditions is chosen as the crystal model. The unit cell contains two atoms of which each atom provides one orbital. A visualization is given in Fig. 12.

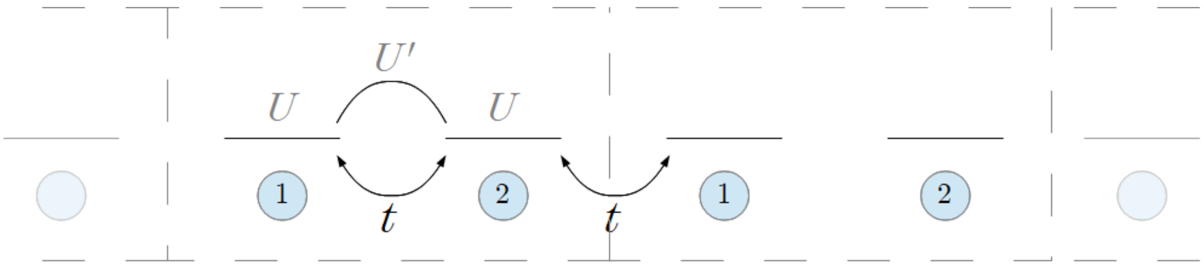

Figure 12: The observed lattice model with hopping parameter t. The Coulomb repulsion between two electrons which occupy the same orbital is governed by U, while U' represents the interaction between two electrons on neighbouring orbitals.

Tunneling between the orbitals is governed by a hopping parameter t and the unit cell length is $2a$. In the numerical calculations a is set to 1 because the dependence on this parameter is not of interest in this project. The model was examined at half-filling and zero temperature, because at non-zero temperature the problem would become more difficult due to an increase of the electrons' kinetic energy. It was selected due to its simplicity and it can easily be mapped on the Hubbard dimer for the atomic model. In this project, the GWA is performed under the G^0W^0 scheme, i.e. for the first iteration of Hedin's equations the Green's function is considered in its non-interacting case G^0 to calculate the screened potential W^0 and self-energy, as described in the next section. Therefore, the following non-interacting Hamiltonian matrix was set up for the model after moving to k-picture:

$$H(k) = \begin{pmatrix} \mu & t(1+e^{2ika}) \\ t(1+e^{-2ika}) & \mu \end{pmatrix} . \tag{34}$$

The *Linear Algebra PACKage* (LAPACK [13]) was used to diagonalize the Hamiltonian matrix and obtain its eigenvectors and -values for a discrete k-mesh and band indices n. Taking a look at the eigenvalues $\epsilon_{1,2} = \mu \pm 2tcos(ak)$ shows two bands with cosine shape as seen in Fig. (13).

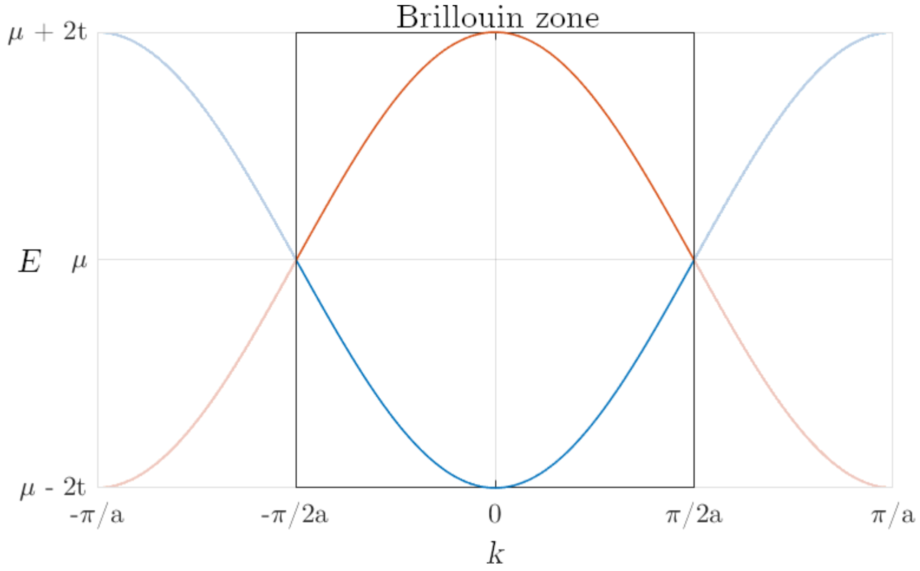

Figure 13: Bandstructure of the model shown in Fig. 12 in the non-interacting case.

4.2 GW procedure

With the eigenvalues and eigenstates of the non-interacting lattice Hamiltonian a one-shot GWA, i.e. only one calculation iteration, was performed. This decreases the computational effort but also makes the results non-self-consistent. The approximation is done numerically on a k-mesh containing N_k discrete k-values, spanning the Brillouin zone from $-\pi/2a$ to $+\pi/2a$. The computation scheme was performed according to [1] and will be roughly delineated here. The first quantity to be calculated is the polarization. By plugging in G^0 from Eq. (13) into Eq. (22) the polarization can be written as:

$$P^0(r,r';\omega) = \sum_{kn}^{occ}\sum_{k'n'}^{unocc}\left(\frac{\psi_{kn}(r)\psi^*_{kn}(r')\psi_{k'n'}(r')\psi^*_{k'n'}(r)}{\omega-\epsilon_{k'n'}+\epsilon_{kn}+i\delta}\right.$$
$$\left.-\frac{\psi_{k'n'}(r)\psi^*_{k'n'}(r')\psi_{kn}(r')\psi^*_{kn}(r)}{\omega+\epsilon_{k'n'}-\epsilon_{kn}-i\delta}\right) \quad . \tag{35}$$

By introducing a minimal basis $\{B_{ki}\}$, normalized and satisfying Bloch's theorem, the polarization can be expanded according to

$$P(r,r';\omega) = \sum_{kij} B_{ki}(r)P_{ij}(k,\omega)B^*_{kj}(r') \tag{36}$$

with the basis index $i = \{\alpha\beta\}$ where the bare Coulomb interaction is

$$v_{ij}(k) = U_{\alpha\beta,\alpha'\beta'} = \int d3d4\,\underbrace{\phi_\alpha(3)\phi_\beta(3)}_{B_i(3)}\,U(3,4)\,\underbrace{\phi_{\alpha'}(4)\phi_{\beta'}(4)}_{B_j(4)} \quad . \tag{37}$$

The numerators may then be rewritten as

$$\begin{aligned}\psi_{kn}(r)\psi^*_{k'n'}(r) &= \sum_{\alpha\beta}\chi_{k\alpha}(r)c_{\alpha n}(k)\chi_{k'\beta}(r)c^*_{\beta n'}(k')\\ &= \sum_{\alpha\beta}\sum_{T,T'}e^{i\vec{k}\vec{T}}e^{-i\vec{k}'\vec{T}'}\varphi_\alpha(\vec{r}-\vec{T})\varphi^*_\beta(\vec{r}-\vec{T}')c_{\alpha n}(k)c^*_{\beta n'}(k')\\ &= \sum_{\alpha\beta}\underbrace{\sum_{T}e^{i(\vec{k}-\vec{k}')\vec{T}}\varphi_\alpha(\vec{r}-\vec{T})\varphi^*_\beta(\vec{r}-\vec{T})}_{B_{qi}(r):=B_{k'-k,\alpha\beta}(r)}c_{\alpha n}(k)c^*_{\beta n'}(k')\end{aligned}$$

where the sums go over the product basis indices α and β, as well as lattice vector $\vec{T}$. The polarization can then be represented by the following matrix:

$$\begin{aligned}P_{ij}(q,\omega) = \frac{1}{N_k}\sum_{spin}\sum_{k}\sum_{n}^{occ}\sum_{n'}^{unocc}&\langle B_{qi}\psi_{kn}|\psi_{k+q,n}\rangle\langle\psi_{k+q,n'}|\psi_{kn}B_{qj}\rangle\\ \times&\left(\frac{1}{\omega-\epsilon_{k+q,n'}+\epsilon_{kn}+i\delta}-\frac{1}{\omega+\epsilon_{k+q,n'}-\epsilon_{kn}-i\delta}\right)\ .\end{aligned}$$

Other quantities can be expanded analogously. The response function is then deduced from the polarization via the schematic matrix equation

$$R = (1-Pv)^{-1}P\ . \tag{38}$$

The self-energy calculation is split into its frequency-independent exchange and frequency-dependent correlation parts. The screened interaction is split accordingly into the bare Coulomb potential $v(q)$ and the correlation part of the screened potential $W^c(q,\omega)$

$$W = v + vRv = v + W^c\ . \tag{39}$$

The exchange part of the self-energy may be calculated according to

$$\Sigma^x_n(q) = -\sum_{k}\sum_{n'}^{occ}\sum_{ij}\langle\psi_{qn}\psi_{k-q,n'}|B_{ki}\rangle\, v_{ij}(k)\,\langle B_{kj}|\psi_{k-q,n'}\psi_{qn}\rangle \tag{40}$$

and the spectral function of the self-energy's correlation part according to

$$\Gamma_n(q,\omega) = \begin{cases}\sum_{kn'}^{occ}\sum_{ij}\langle\psi_{qn}\psi_{k-q,n'}|B_{ki}\rangle\, D_{ij}(k,\epsilon_{k-q,n'}-\omega)\\ \qquad\times\langle B_{kj}|\psi_{k-q,n'}\psi_{qn}\rangle\,\Theta(\epsilon_{k-q,n'}-\omega) & \text{for } \omega\le\mu\\ \\ \sum_{kn'}^{unocc}\sum_{ij}\langle\psi_{qn}\psi_{k-q,n'}|B_{ki}\rangle\, D_{ij}(k,\omega-\epsilon_{k-q,n'})\\ \qquad\times\langle B_{kj}|\psi_{k-q,n'}\psi_{qn}\rangle\,\Theta(\omega-\epsilon_{k-q,n'}) & \text{for } \omega\ge\mu\end{cases}\ . \tag{41}$$

Here the spectral function of the screened potential

$$D_{ij}(q,\omega) = -\frac{1}{\pi}Im(W_{ij}(q,\omega))sgn(\omega) \tag{42}$$

was introduced. Since the numerical calculations are based on a discrete frequency mesh, a linear interpolation was performed for the varying energy arguments for D in Eq. (41). From Γ, the correlation part of the self-energy was determined and lastly, the resulting self-energy is simply the sum of the exchange and correlation parts

$$\Sigma^{GW}_n(q,\omega) = \Sigma^x_n(q) + \Sigma^c_n(q,\omega)\ . \tag{43}$$

4.3 Hubbard I Approximation

To apply the Hubbard I approximation, the self-energy of the atomic model of interest needs to be found. Due to the simpleness of the examined model in this project, this was done analytically. The model is described as follows:

Consider a unit cell consisting of two atoms with one orbital each. The electrons which occupy the orbitals may hop between sites and also interact with each other. The orbitals may also have differing potentials. This model is usually referred to as the Hubbard dimer and can be described through the following Hamiltonian, based upon the Hubbard model:

$$\hat{H} = \sum_{i}^{2} \hat{n}_i \epsilon_i + t \sum_{\langle ij \rangle, \sigma}^{2} \hat{c}_{i\sigma}^{\dagger} \hat{c}_{j\sigma} + \sum_{i}^{2} U_i \hat{n}_{i\uparrow} \hat{n}_{i\downarrow} + U' \hat{n}_1 \hat{n}_2 \ .$$

The first term describes the on-site potentials ϵ_i where it is $\hat{n}_i = \hat{n}_{i\uparrow} + n_{i\downarrow}$. Hopping between the two sites is described by the second term, while the third one handles the on-site Coulomb interaction between electrons. The last term describes the Coulomb interaction of electrons on two different sites. Assuming that all orbitals have the same on-site potential $\epsilon_i = 0 \ \forall \ i$ and the same on-site Coulomb strength $U = U_i \ \forall \ i$, the model may be schematized as in Fig (14).

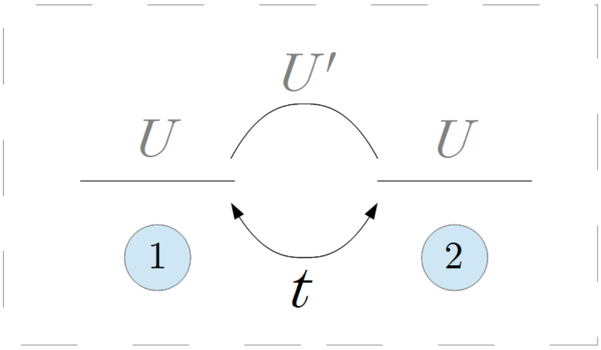

Figure 14: The Hubbard dimer with orbitals of the same potential and same on-site Coulomb strength U. Hopping is governed by t while U' represents the Coulomb interaction between the sites. The numbers 1 and 2 denote the two sites.

This model is used for the Hubbard I approximation as the atomic counterpart to the crystal model from Fig. (12). A full analytic determination of the Green's function can be found in Appendix 8.1. The solution in the orbital basis (1,2) at *half-filling* is

$$\begin{aligned} G_{ij,\sigma}(\omega) = & \frac{(\frac{b+a}{2})^2}{\omega + t - \epsilon_0 - i\delta} + \frac{(-1)^{i+j}(\frac{b-a}{2})^2}{\omega - t - \epsilon_0 - i\delta} \\ & + \frac{(\frac{b-a}{2})^2}{\omega - (U + 2U' - t) + \epsilon_0 + i\delta} + \frac{(-1)^{i+j}(\frac{b+a}{2})^2}{\omega - (U + 2U' + t) + \epsilon_0 + i\delta} \end{aligned} \tag{44}$$

with the ground state energy

$$\epsilon_0 = \frac{1}{2}(U' + U - \sqrt{(U' - U)^2 + 16t^2}) \tag{45}$$

$$\text{where} \quad a = \frac{\epsilon_0 - U}{\sqrt{(\epsilon_0 - U)^2 + 4t^2}} \quad \text{and} \quad b = \frac{2t}{\sqrt{(\epsilon_0 - U)^2 + 4t^2}} \ .$$

Through this and the Dyson equation (Eq. 18) the atomic self-energy may be determined. Plots of the spectral function of the Green's function and self-energy are shown in Fig. (15).

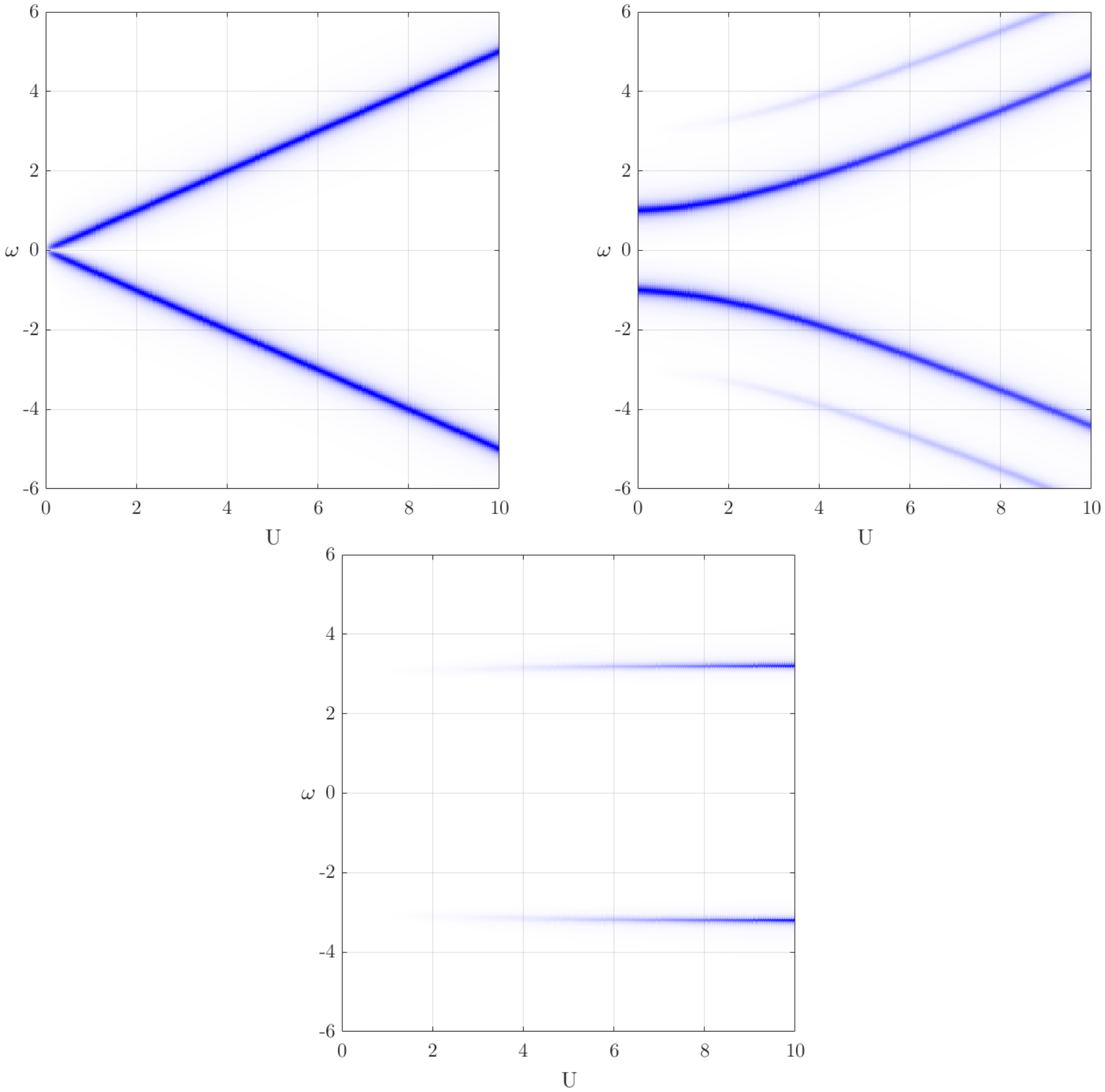

Figure 15: Spectral functions of the atomic Green's function for $t = 0$ (left) and $t = 1$ (right). The graph at the bottom shows the spectral function of the atomic self-energy for $t = 1$.

The frequency ω is on the y-axis, while the Coulomb parameter U is on the x-axis. It is set $U' = U/10$, $t = 1$ and $\delta = 0.1$. The pole structure of the Green's function as seen in the left graph corresponds to combinations of the Hamiltonian's eigenstates. For $t = 0$ two peaks scale linearly with U. For non-zero t two subbands, called Hubbard bands, appear with a distance of $\approx U$ between them. Furthermore, it is noted that the atomic self-energy does not change in frequency with U, but only increases its intensity.

4.4 Double counting

Now that the self-energies of the crystal and atomic model were determined they can be summed together. As the two models contain partially overlapping interaction terms the problem of double-counting arises which can be compensated through the subtraction of an additional term Σ^{dc}:

$$\Sigma(k) = \Sigma^{GW}(k) + \Sigma^{at} - \Sigma^{dc} \ . \tag{46}$$

There are several ways through which the double-counting term can be constructed. In this project three approaches were inspected and compared. The first is applying the GWA to the atomic problem as well. This was done analytically, as shown in Appx. (8.2). The following solution for the self-energy was reached:

$$\Sigma^{dc} = \Sigma_{ij}^{at,GW}(\omega) = -(-1)^{i+j}\frac{U_{ij}}{2} + \frac{a}{4b}\left(\frac{1}{\omega - b - c} + \frac{(-1)^{i+j}}{\omega + b + c}\right) \tag{47}$$

with

$$\begin{aligned} a &= (U-U')^2(-2t + i\delta) \ , \\ b &= -\sqrt{4t^2 + 4(U-U')t} + i\delta \ , \\ c &= -t + i\delta \ . \end{aligned}$$

Similar to the atomic self-energy, rather sharp peaks are to be expected from the analytic solution. Since the term is subtracted, this might cause negative parts in the resulting spectral function of G and thus causality issues. Another reasonable approach to the double-counting is to subtract the local self-energy of the crystal model's GWA solution:

$$\Sigma^{dc} = \Sigma_{ij}^{GW,loc}(\omega) = \frac{1}{N_k}\sum_k \Sigma_{ij}^{GW}(\omega, k) \ . \tag{48}$$

This might raise less causality issues, as the magnitude and broadness will be similar to numerical GW solution of the crystal model. The last approach handled in this project will be about subtracting basically the local GWA self-energy within DMFT. The Green's function of the crystal model's one-shot result will be used to conduct one additional GWA iteration but with the impurity's screened potential W^{imp} instead, i.e.,

$$\begin{aligned} \Sigma^{GW^{imp}}(\omega, k) &= iG^{GW}(\omega, k)W^{imp}(\omega) \ , \\ \Sigma^{dc} = \Sigma_{ij}^{GW^{imp},loc}(\omega) &= \frac{1}{N_k}\sum_k \Sigma_{ij}^{GW^{imp}}(\omega, k) \ . \end{aligned} \tag{49}$$

Similar to the second approach, the magnitude and broadness is expected to be akin to the GWA term.

5 Results

First, the results of the two methods GWA and HIA will be analyzed separately before the combination, to compare where the different structures originate from. Then the three different double-counting variants will be applied and evaluated.

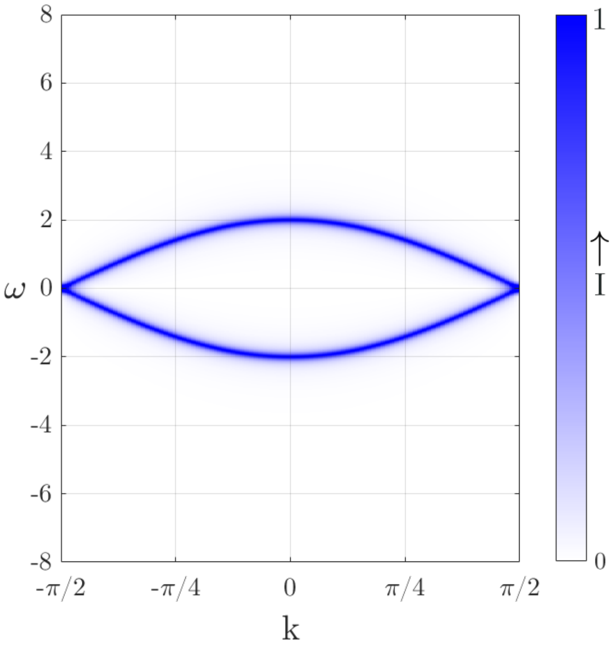

Figure 16: Non-interacting spectral function the lattice model. The color bar shows the intensity I in arbitrary units with a linear scale.

As a reference to the quasi-particle band structure, the non-interacting spectral function of the lattice model is presented in Fig. (16). As can be seen, it agrees with the analytic bandstructure from Fig. (13). The two bands represent quasi-particle energies. At the border of the Brillouin zone ($k = \pm\pi/2$) the bands merge which suggests the model behaves like a metal for $U = U' = 0$.

5.1 Atomic self-energy combined with lattice G^0

Next, the effects of the Hubbard I approximation were observed, by inserting the local atomic self-energy Σ^{at} and the non-interacting Green's function G^0 of the lattice model into the Dyson equation (Eq. 18):

$$G(k;\omega) = [G^0(k;\omega)^{-1} + \Sigma^{at}(\omega)]^{-1} \ . \tag{50}$$

Plots of the resulting spectral function for various values of U can be seen below:

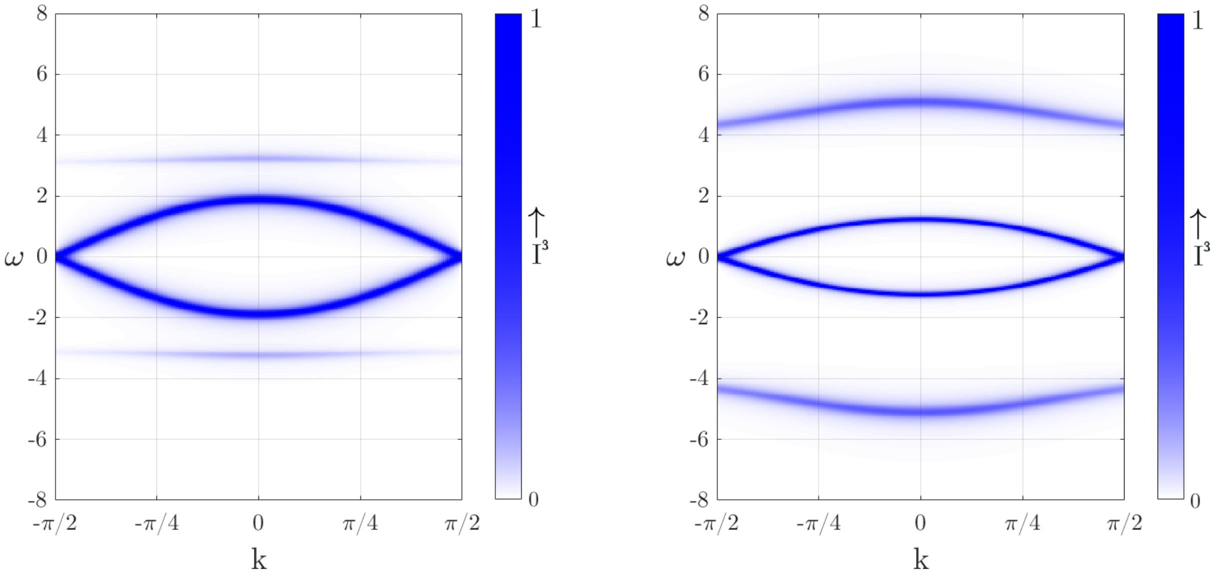

Figure 17: Spectral functions of the atomic self-energy combined with the lattice G^0 for $U = 1, U' = 0.1$ (left) and $U = 4, U' = 0.4$ (right). The hopping parameter t was set to 1 for both graphs. The color bar shows the intensity I^3 in arbitrary units.

Quasi-particle peaks comparable to the non-interacting graph in Fig. (16) are visible. With increasing on-site interaction U the bands narrow down towards the Fermi energy at $\mu = 0$, since electrons become less likely to doubly occupy and thus less likely to hop. The system becomes more atomic-like. With a distance of about U to the quasi-particle bands, satellite structures from the multiplet states of the Hubbard dimer can be seen, which show only weak dispersion for low U, becoming stronger with increasing on-site repulsion. The weight of the satellites compared to the quasi-particle peaks also increases slightly with higher U. A view of the cross-section at the Γ-point of the $U = 4$ plot is presented in Fig. (18) below.

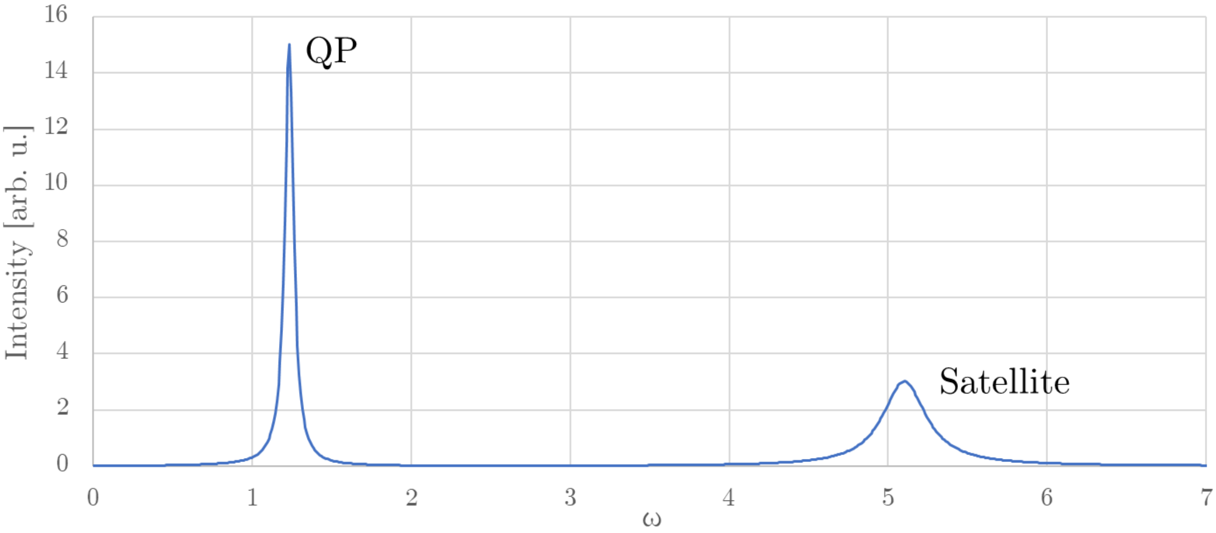

Figure 18: Spectral function for $U = 4, U' = 0.4, t = 1$ at the Γ-point.

The width of the peaks reflects the lifetime of the particles, as depicted in Eq. (16). Though, in the numerical calculations a smearing at the poles enters through a non-zero $i\delta$-value, like in Eq. (35). A δ-value of 0.1 was chosen for this project. Thus, the width is only qualitatively correct. Nevertheless, it can be observed that the satellite peak is much broader than the quasi-particle peak due to the atomic self-energy.

5.2 One-shot GWA

This section shows plots of the GWA by inserting the self-energy Σ^{GW} of the calculation into the Dyson equation (Eq. 18):

$$G(k;\omega) = [G^0(k;\omega)^{-1} + \Sigma^{GW}(k;\omega)]^{-1} \; . \tag{51}$$

In Fig. (19) below, the spectral function of the screened potential W and the self-energy is presented.

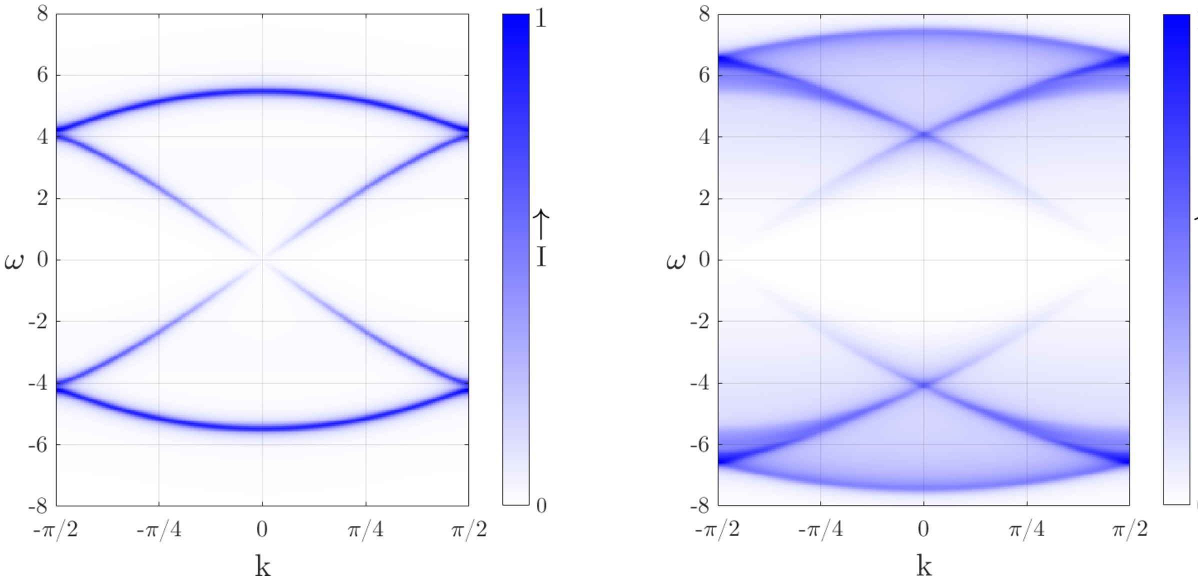

Figure 19: Spectral function of the screened potential W_{11} (left) and spectral function of the self-energy Σ^{GW} (right) for $U = 4, U' = 0.4, t = 1$.

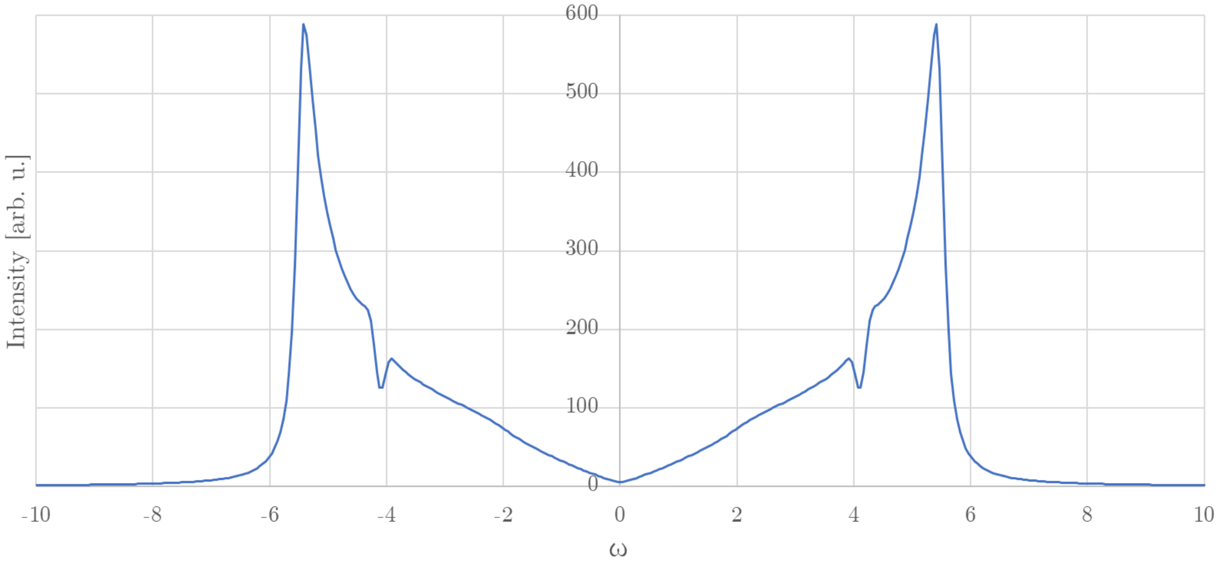

Figure 20: Spectral function of the local screened potential W_{11}^{loc} for $U = 4, U' = 0.4, t = 1$.

The poles of the single-particle excitations have been shifted due to interactions and can be interpreted as plasmons in the spectral function of the screened potential (left). Another depiction of this is in the graph of the local screened potential (bottom). The poles are then convoluted according to Eq. (41) in the plot of the self-energy's spectral function on the right. Since the calculations were done at half-filling, the plot is symmetric about the Fermi-energy (= 0) as expected – electrons and holes behave equivalently in this model. Below in Figs. (21 to 23) the imaginary part of the self-energy for $U = 4$ is shown for three k-points.

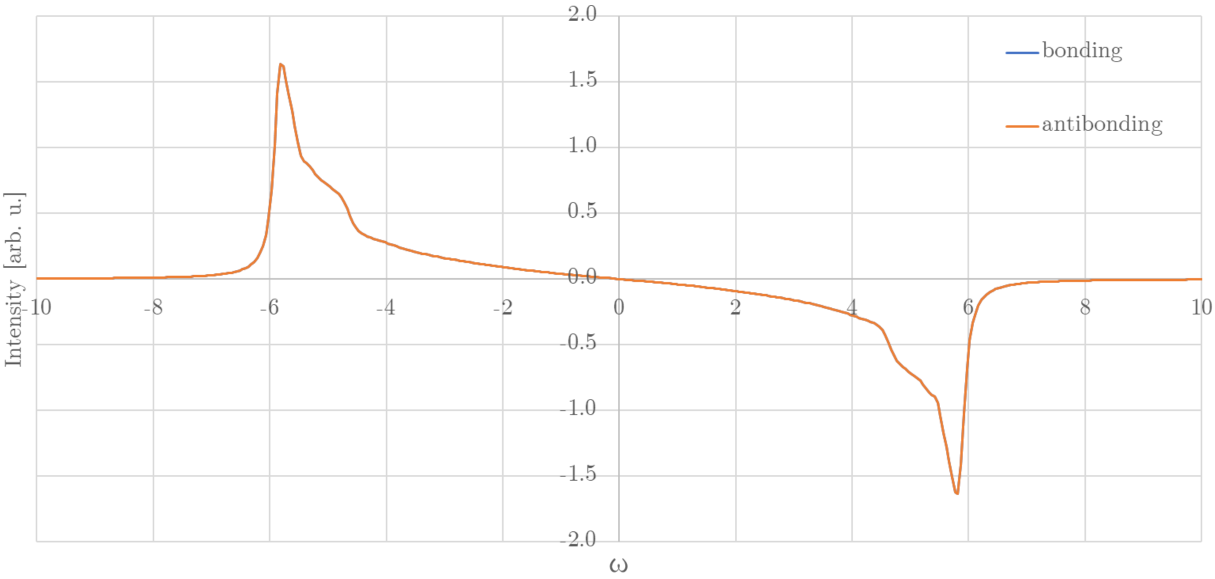

Figure 21: $\mathrm{Im}(\Sigma^{GW})$ for $U = 4$ at the border of the Brillouin zone. The bonding and antibonding graphs overlap. Bonding and antibonding states arise through the overlap between two orbitals due to which the states split in the lower energy bonding and higher energy antibonding state

[4].

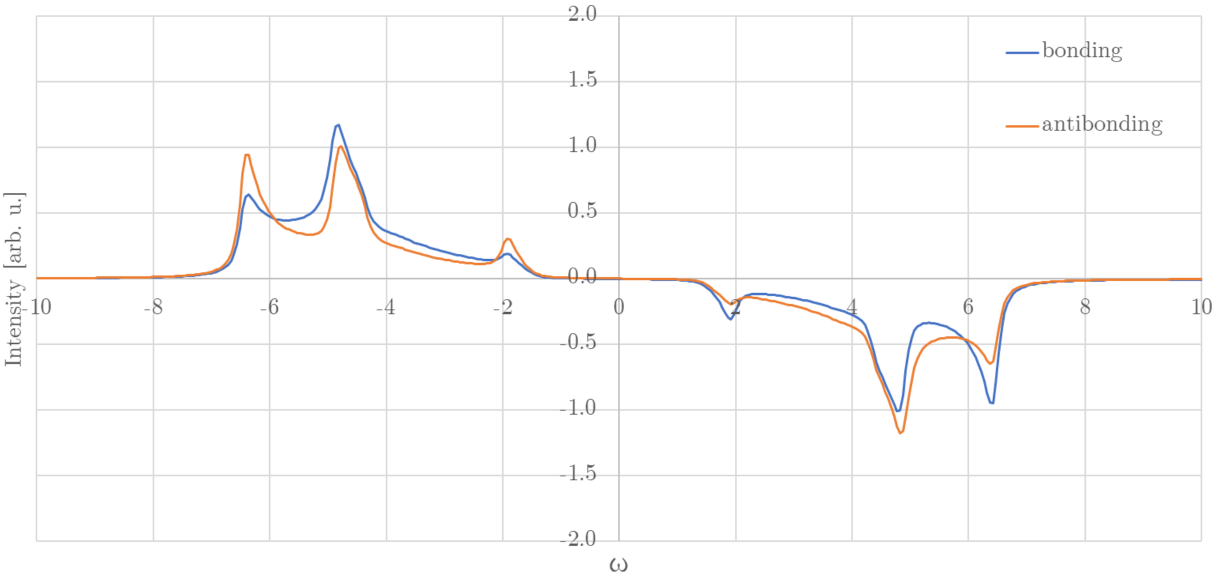

Figure 22: $\mathrm{Im}(\Sigma^{GW})$ for $U = 4$ at $k = -\pi/4$, between the Brillouin zone border and the Γ-point.

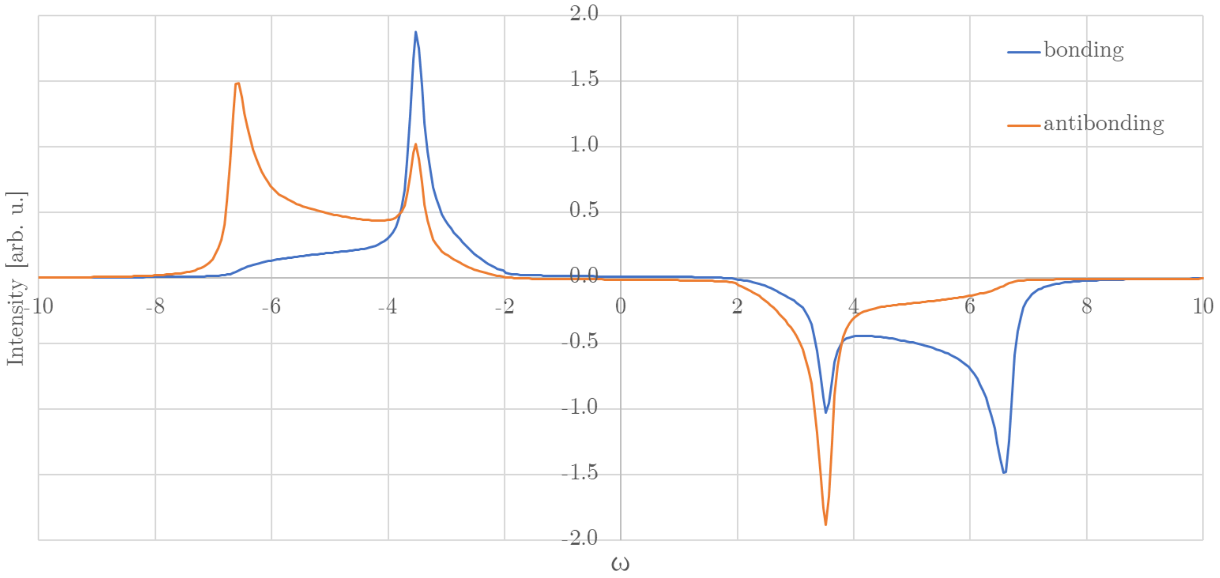

Figure 23: Im(Σ^{GW}) for $U = 4$ at the Γ-point.

The resulting spectral function of the Green's function within the GWA is presented in Fig. (24) below:

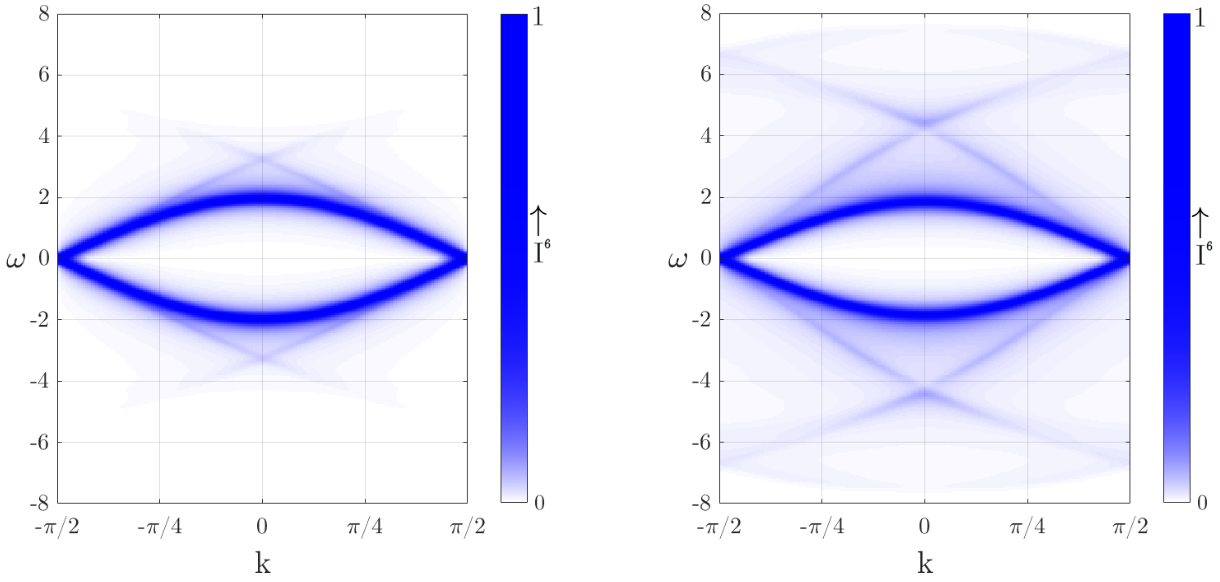

Figure 24: Spectral function of G^{GW} for $U = 1, U' = 0.1$ (left) and $U = 4, U' = 0.4$ (right). The hopping parameter t was set to 1 for both graphs. The color bar shows the intensity I^6 in arbitrary units.

The quasi-particle bands narrow slightly inwards with increasing U, but less so than in the atomic graphs from Fig. (17), because the screening effect is incorporated. In the regions above the upper and below the lower quasi-particle features, the plasmon structure in form of satellites becomes visible. It should be noted that the GWA overestimates the energy of plasmon features [5].

5.3 GW + Hubbard I without double-counting correction

The resulting spectral function of the combination GWA+HIA without correcting for double-counting according to

$$G(k;\omega) = [G^0(k;\omega)^{-1} + \Sigma^{GW}(k;\omega) + \Sigma^{at}(\omega)]^{-1} \tag{52}$$

can be seen in Fig. (25) below.

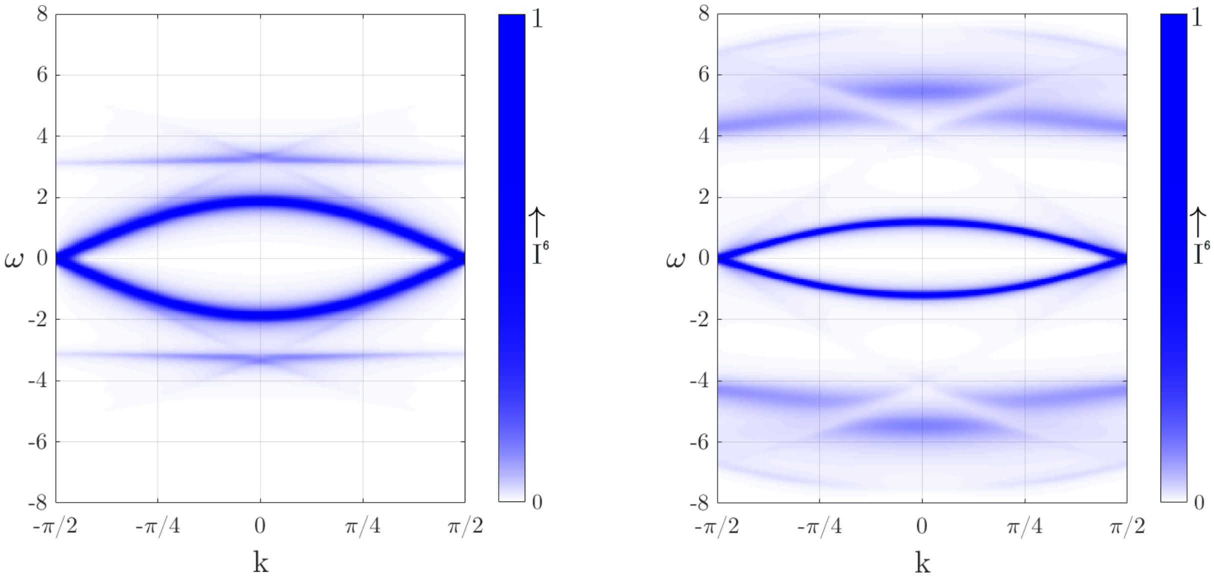

Figure 25: Spectral function of G^{GW+HI} for $U = 1, U' = 0.1$ (left) and $U = 4, U' = 0.4$ (right). The hopping parameter t was set to 1 for both graphs. The color bar shows the intensity I^6 in arbitrary units.

With increasing on-site Coulomb repulsion U, the quasi-particle peaks narrow more quickly than in the atomic result (Fig. 17). Moreover, the plasmon structure from the GW result can be seen here, as it mixes with the satellites from the atomic result.

5.4 Double counting

Now the different double-counting terms will be observed. Below in Fig. (26) a plot of the bonding elements of the self-energies' imaginary part at the Γ-point of the Brillouin zone is shown.

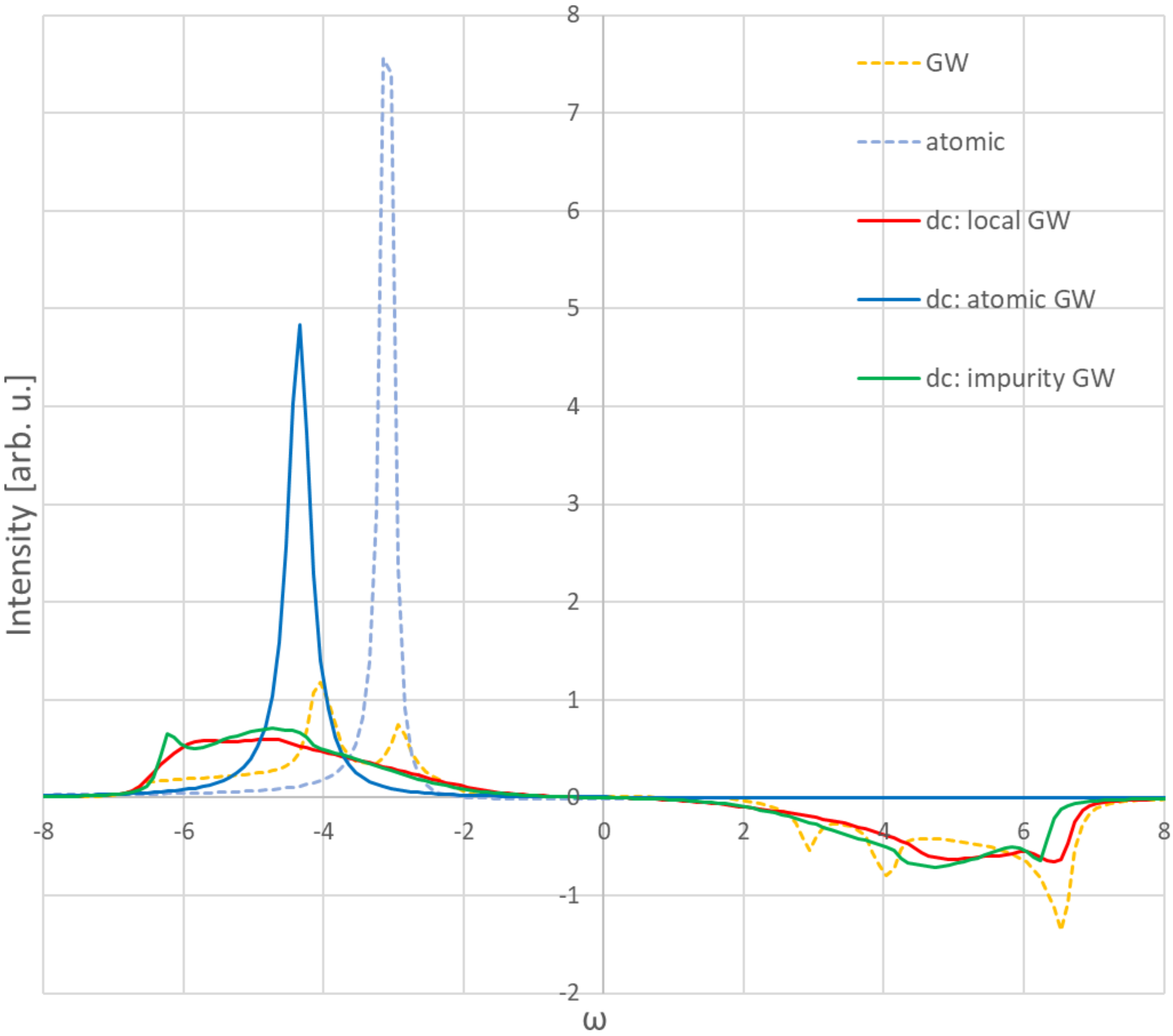

Figure 26: Different double-countings (dc) at Γ-point for $\mathrm{Im}(\Sigma_{BB})$ for $U = 2$

It becomes immediately clear, that the atomic GW double-counting will have problems with causality violation, as the amplitude of the peak surpasses the $\Sigma^{GW} + \Sigma^{at}$ self-energies, and thus will yield a negative spectral function. Both the local and impurity double-counting have this issue too in the region $\omega = [-7, -4.5]$, but to a smaller extent. Moreover, they have very similar intensities. It should be noted, that since the calculations were not done self-consistently, a certain arbitrariness enters the data of the GW, local GW and impurity GW plot.

5.4.1 Local GW as double-counting

Spectral functions with the local GW self-energy subtracted for double-counting are presented in Fig. (27) below.

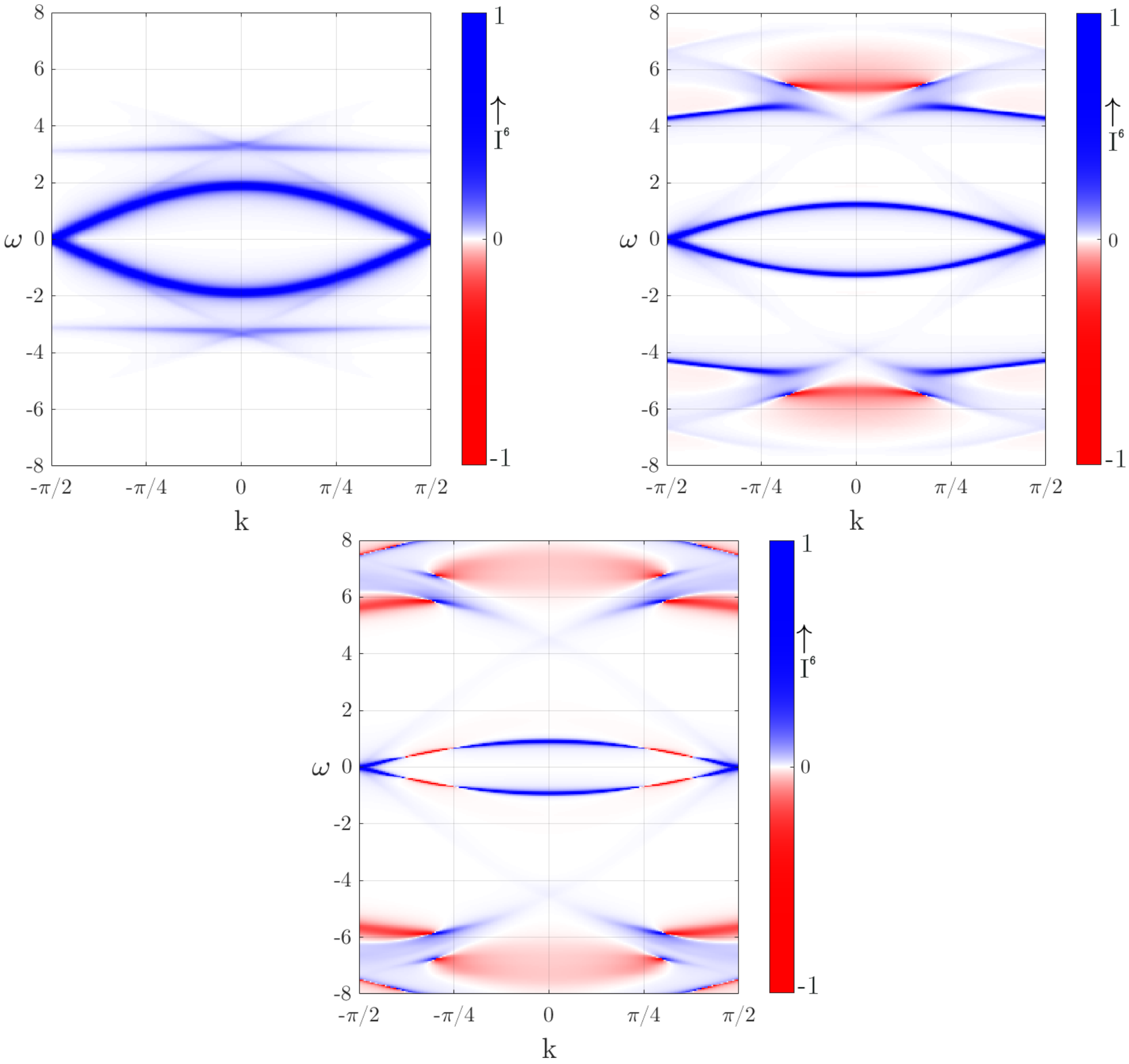

Figure 27: Spectral functions of GW+HI with subtracted local GW as double-counting for $U = 1, U' = 0.1$ (left), $U = 4, U' = 0.4$ (right) and $U = 6, U' = 0.6$ (bottom). The color bar shows the intensity I^6 in arbitrary units.

The satellites of the atomic and of the GW results mix again, but the structure of the GW calculation is weakened slightly. With self-consistent calculations, the plasmon structures might combine towards the satellites of the atomic calculation. Causality issues appear around the plasmon satellites for increased $U = 4$ and also around the quasi-particle structure with even higher value of $U = 6$. Moreover, the graphs show no Mott-Hubbard transition with increasing U, as it was expected in the half-filled one-dimensional case [15]. This makes sense, since there is no coupling between the atomic (Hubbard bands) and GW calculations (quasi-particle bands), as it would be within full DMFT calculations. The quasi-particle structure is similar to GWA+HIA from Fig. (25) but the bands do narrow less quickly with increasing U, as can be compared in Fig. (28) below.

This shows that the screening effect is incorporated, which weakens the interaction, and double-counting is accounted for.

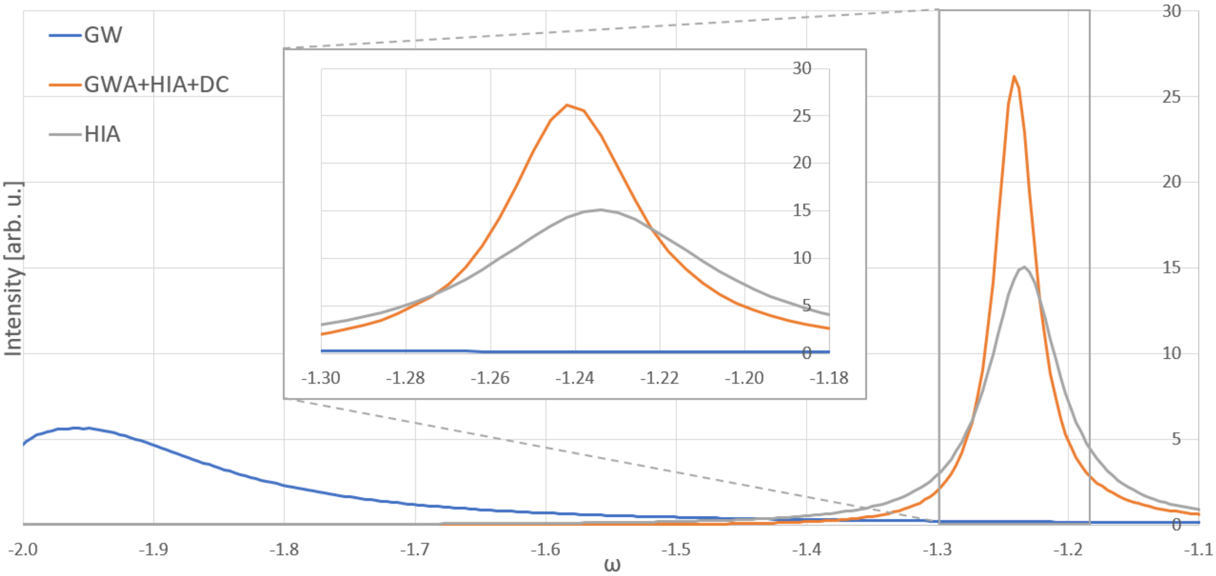

Figure 28: Comparison of the spectral functions' quasi-particle peaks for $U = 4$ at the Γ-point.

To understand how the spectral function results from the self-energy, it is helpful to take a look at Eq. (17). For small values of $\omega - \epsilon_{kn} - \mathrm{Re}(\Sigma_{kn}(\omega)$ and $\mathrm{Im}(\Sigma_{kn})$ peaks will occur in the spectral function. Thus, one can look for intersections of the two functions $\mathrm{Re}(\Sigma)$ and $\omega - \epsilon_{kn}$ for which $\mathrm{Im}(\Sigma)$ is small to roughly predict the peak structure of the spectral function. A descriptive example of the bonding element is presented in Fig. (29), with the corresponding imaginary parts of the self-energy and Green's function in Fig (30).

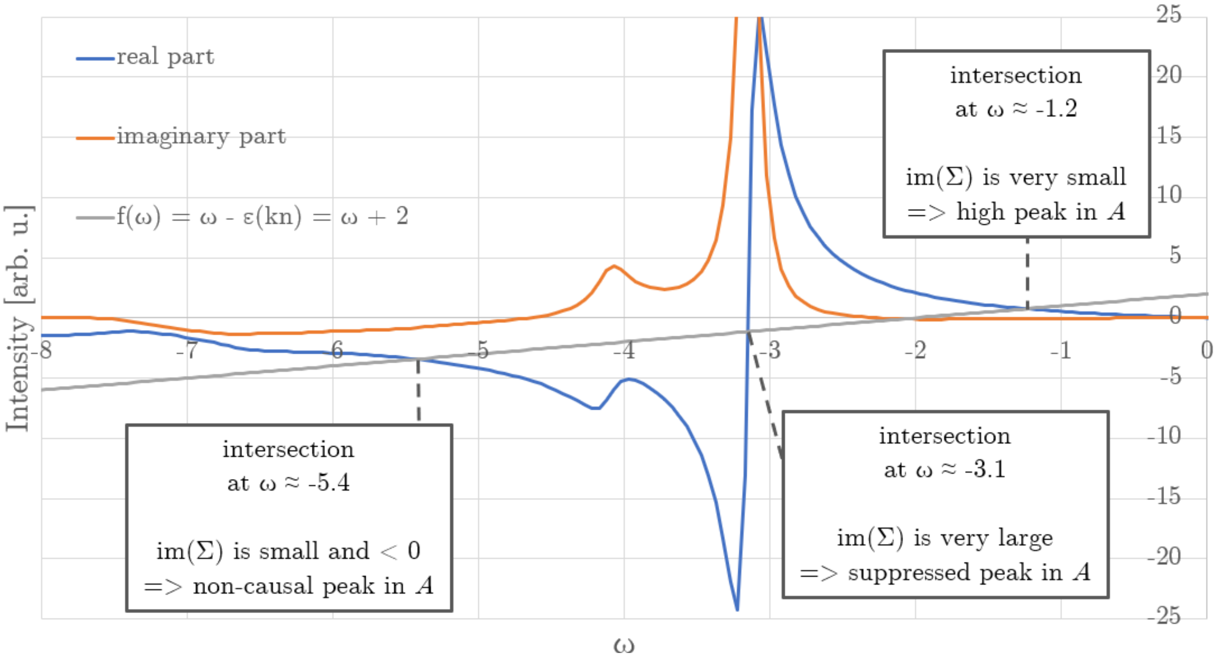

Figure 29: The real and imaginary parts of the self-energy's bonding element at the Γ-point for $U = 4$. The eigenenergy of the bonding state at the Γ-point is -2. By looking for intersections with Re(Σ) one can predict the peak structure of the spectral function A through Eq. (17).

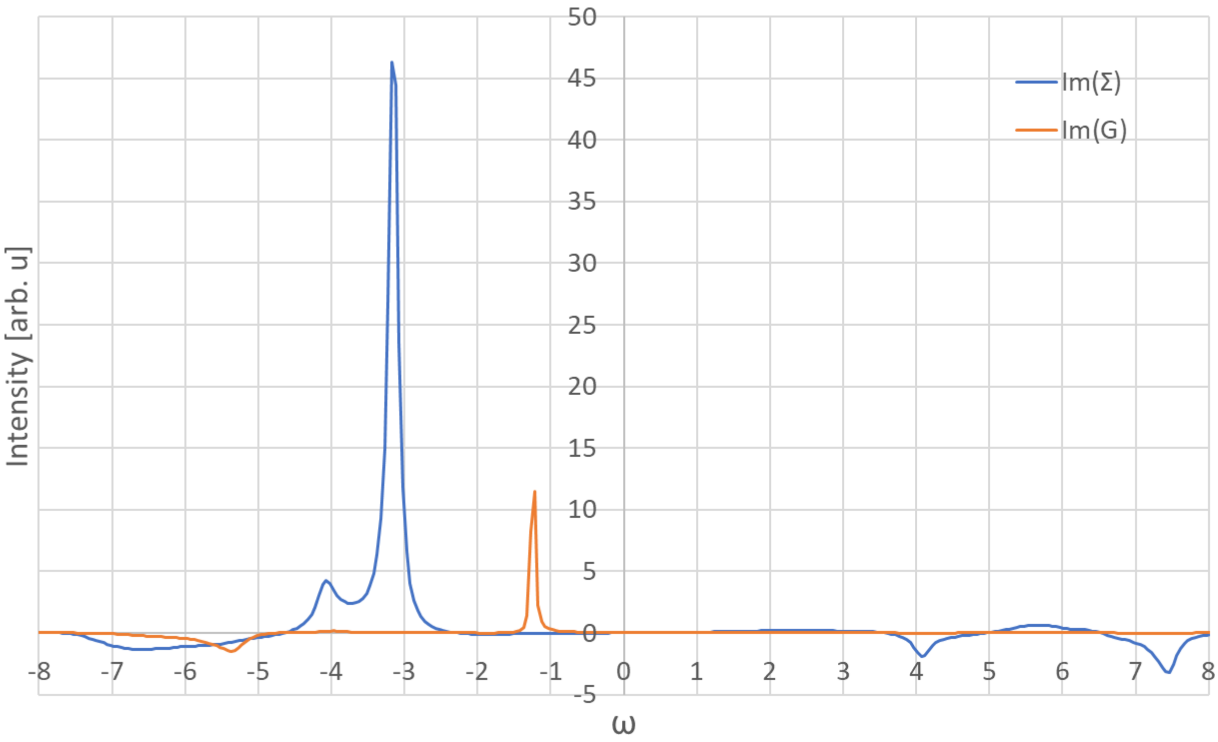

Figure 30: Im(Σ_{BB}) (blue) and Im(G_{BB}) (orange) at the Γ-point for $U = 4$.

5.4.2 Impurity GW as double-counting

Fig. (31) below shows spectral functions with the impurity GW self-energy subtracted to account for double-counting.

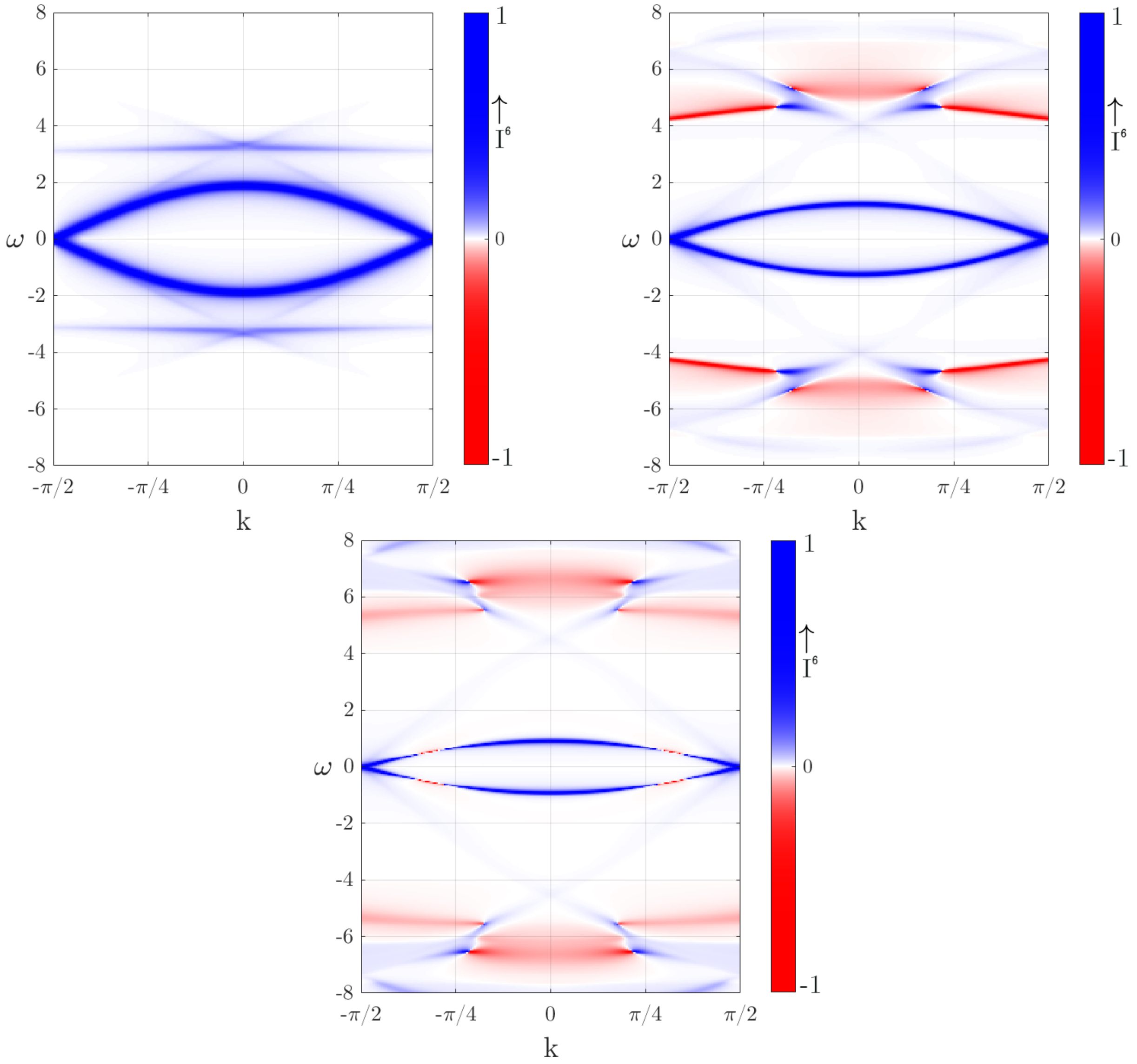

Figure 31: Spectral functions of GW+HI with subtracted impurity GW to account for double-counting for $U = 1, U' = 0.1$ (left) and $U = 4, U' = 0.4$ (right). The color bar shows the intensity I^6 in arbitrary units.

This double-counting approach grants similar results as the local GW double-counting for lower values of U. For higher values, along the same causality issues as in Fig. (27), additional causality violation occurs in the satellite regions of $k < -\pi/4$ and $k > \pi/4$ as the double-counting term increases here with U until it exceeds the GWA+HIA self-energy in absolute values.

5.4.3 Atomic GW as double-counting

Below Fig. (32) shows spectral functions with the atomic GW self-energy subtracted due to double-counting.

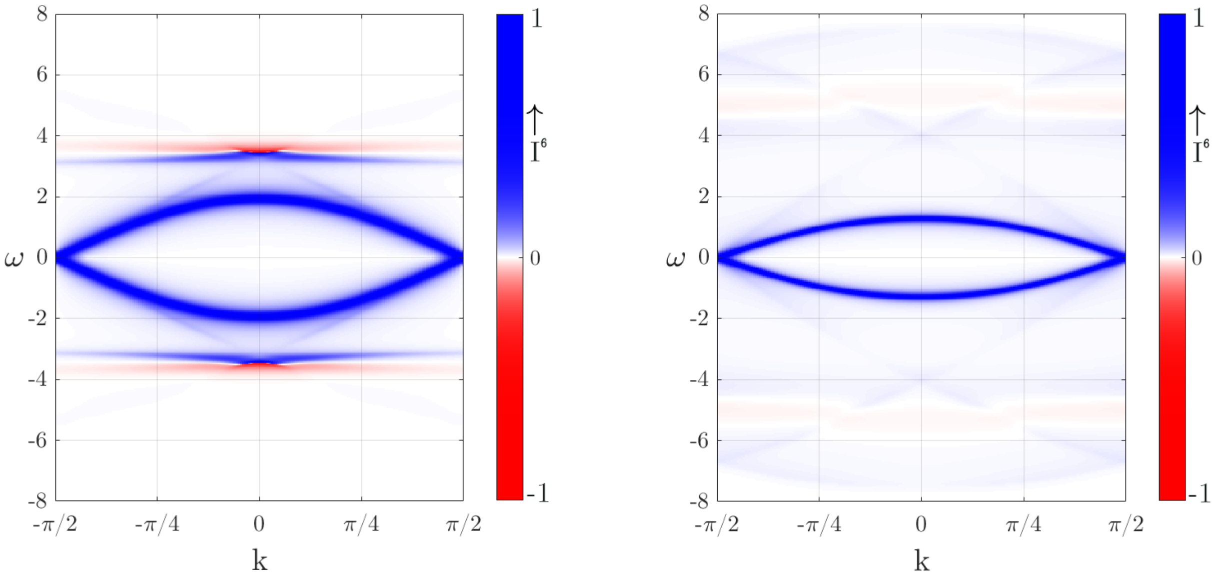

Figure 32: Spectral functions of GW+HI with subtracted atomic GW as double-counting for $U = 1, U' = 0.1$ (left) and $U = 4, U' = 0.4$ (right). The color bar shows the intensity I^6 in arbitrary units.

As expected, this approach already suffers from strong causality violation for low U. Interestingly, structures besides the quasi-particle bands are heavily suppressed for high values of U, which is due to the high amplitude of the imaginary part of the double-counting term, as seen in Fig. (26) before. The satellite and non-causal features are thus still present in the plot, but very heavily suppressed and thus barely visible. Additionally, the quasi-particle band narrows slightly less than in the other double-counting methods.

6 Conclusions

In this project, the GW approximation was combined with the Hubbard I approximation and applied to a one-dimensional Hubbard model in a non-self-consistent way. The spectral function of the resulting Green's function was analyzed with an emphasis on the performance of three different variants to circumvent the double-counting problem of the combination. It was observed that out of the three approaches, subtracting the local self-energy of the GWA result serves best to counteract this problem. In addition to this, it is also the computationally cheapest variant, by just requiring a sum over the k-mesh. In general, it was observed that subtracting self-energy terms to circumvent double-counting for this method leads to non-causal features in the spectral function for Coulomb repulsion values of ≈ 2 and higher. These start to appear outside of the quasi-particle regime at first, until a value of ≈ 6 is reached, at which also the quasi-particle region is affected. The non-causal features become more pronounced with increasing on-site repulsion U. However, performing self-consistent calculations may mitigate this problem, as it was found that in self-consistent GW+EDMFT calculations, physical observables remain causal [20]. Furthermore, the quasi-particle band structure of real materials may be approximated with this method without causality violation through Eq. (15), where only the real part of the self-energy is involved. The quasi-particle structures show influence from both the strong correlation and screening effects, by narrowing with increasing on-site Coulomb repulsion faster than in a pure GWA calculation, but more slowly than in the atomic model. This means that screening effects are included along with local on-site correlations in this method. Plasmon structures of the GWA, which are energetically overestimated [5], are slightly weakened and mix up with the HIA structures. Self-consistent calculations might combine the plasmon features further. Lastly, it can be noted that the one-shot GWA+HIA method is computationally very cheap, e.g., with a runtime of a few minutes for a $k \times \omega$-mesh of 200×800.

7 Outlook

The previous sections showed that subtracting a double-counting term from the self-energy produces non-causal features in the spectral function of the GWA+HIA method. While the quasi-particle regime was only affected for very high values of U, a safe approach to use this method for the calculation of quasi-particle band structures of real materials would be to use Eq. (15), where only the real part enters:

$$E_n^{QP}(k) = \epsilon_n(k) + Re(\Sigma_n(k)) \ .$$

An approach to construct a positive definite spectral function through diagrammatic expansion as presented in [25] could be considered for further methods in the future. Furthermore, it was noted, that the (energetically overestimated) plasmon structure of the GWA slightly combines with the ones from the HIA. An approach to mitigate the influence of the GWA in this regard could be to introduce a static self-energy in the GWA calculations, effectively a mean-field approximation, to reduce the collective excitations of the plasmon structure. An important step which could improve both of the problems mentioned above, is to do a fully self-consistent calculation, by performing the GWA loop with the self-energy result of the one-shot GWA+HIA method. A simple model was treated in this project for which the atomic part could be solved analytically. To handle more complex models, future improvements should thus involve a numerical solver for the atomic part of the method. Finally, the application of the method to real materials would be another consequent next step.

8 Appendices

8.1 The atomic problem - solved exactly

The considered Hamiltonian is:

$$\hat{H} = \sum_{i}^{2} \hat{n}_i \epsilon_i + t \sum_{\langle ij \rangle, \sigma}^{2} \hat{c}_{i\sigma}^{\dagger} \hat{c}_{j\sigma} + \sum_{i}^{2} U_i \hat{n}_{i\uparrow} \hat{n}_{i\downarrow} + U' \hat{n}_1 \hat{n}_2$$

This model will now be solved analytically to get the exact Green's function G at half-filling with disordered states in the orbital basis. At *half-filling*, the following six states are possible for this model:

$$\begin{aligned}
|1\rangle &= |\uparrow \cdot \downarrow\rangle = \hat{c}_{1\uparrow}^{\dagger} c_{2\downarrow}^{\dagger} |0\rangle \\
|2\rangle &= |\downarrow \cdot \uparrow\rangle = \hat{c}_{1\downarrow}^{\dagger} c_{2\uparrow}^{\dagger} |0\rangle \\
|3\rangle &= |\uparrow\downarrow \cdot\rangle = \hat{c}_{1\uparrow}^{\dagger} c_{1\downarrow}^{\dagger} |0\rangle \\
|4\rangle &= |\cdot \uparrow\downarrow\rangle = \hat{c}_{2\uparrow}^{\dagger} c_{2\downarrow}^{\dagger} |0\rangle \\
|5\rangle &= |\uparrow \cdot \uparrow\rangle = \hat{c}_{1\uparrow}^{\dagger} c_{2\uparrow}^{\dagger} |0\rangle \\
|6\rangle &= |\downarrow \cdot \downarrow\rangle = \hat{c}_{1\downarrow}^{\dagger} c_{2\downarrow}^{\dagger} |0\rangle
\end{aligned}$$

Only the system is assumed to have a total spin of $M = 0$, thus the last two states $|5\rangle$ and $|6\rangle$ are not considered in further calculations. Moreover, it is assumed that both sites have the same potential $\epsilon_1 = \epsilon_2 = 0$.

To solve this model exactly, the Hamiltonian matrix is set-up:

$$H = \begin{pmatrix} U' & 0 & t & t \\ 0 & U' & -t & -t \\ t & -t & U & 0 \\ t & -t & 0 & U \end{pmatrix} \tag{53}$$

Since the descriptive Hamiltonian contains no spin flip terms or double hoppings the transitions states of $\langle 1| H |2\rangle$ and $\langle 3| H |4\rangle$ are all zero. To solve this eigenvalue problem, Löwdin's downfolding technique is applied. Firstly, the eigenvalue problem is written in the following block form

$$\begin{pmatrix} A_{11} & A_{12} \\ A_{21} & A_{22} \end{pmatrix} \begin{pmatrix} v_1 \\ v_2 \end{pmatrix} = \epsilon \begin{pmatrix} v_1 \\ v_2 \end{pmatrix} \tag{54}$$

Where the effective eigenvalue equation for the two subspaces v_1 and v_2 can be determined to be

$$\begin{aligned}
A_{11} v_1 + A_{12} v_2 &= \epsilon v_1 \\
A_{21} v_1 + A_{22} v_2 &= \epsilon v_2
\end{aligned}$$

$$\Rightarrow (A_{11} + A_{12}(\epsilon - A_{22})^{-1} A_{21}) v_1 = \epsilon v_1 \tag{55}$$

$$\Rightarrow (A_{22} + A_{21}(\epsilon - A_{11})^{-1} A_{12}) v_2 = \epsilon v_2 \tag{56}$$

Applying this to the Hamiltonian matrix from (53), results in the following block elements:

$$A_{11} = U' \begin{pmatrix} 1 & 0 \\ 0 & 1 \end{pmatrix} \qquad A_{12} = t \begin{pmatrix} 1 & 1 \\ -1 & -1 \end{pmatrix} \qquad A_{21} = t \begin{pmatrix} 1 & -1 \\ 1 & -1 \end{pmatrix} \qquad A_{22} = U \begin{pmatrix} 1 & 0 \\ 0 & 1 \end{pmatrix}$$

Eq. (55) thus yields:

$$\left[U' \begin{pmatrix} 1 & 0 \\ 0 & 1 \end{pmatrix} + \frac{2t^2}{\epsilon - U} \begin{pmatrix} 1 & -1 \\ -1 & 1 \end{pmatrix} \right] v_1 = \epsilon v_1$$

$$\begin{pmatrix} a + U' & -a \\ -a & a + U' \end{pmatrix} v_1 = \epsilon v_1 \quad , \; a \equiv \frac{2t^2}{\epsilon - U}$$

and thus $\epsilon = (a + U') \pm a$ or:

$$\epsilon_{1,2} = \frac{1}{2} \left(U + U' \pm \sqrt{(U - U')^2 + 16t^2} \right) \qquad \epsilon_3 = U' \tag{57}$$

In an analogous matter for Eq(56):

$$\left[U \begin{pmatrix} 1 & 0 \\ 0 & 1 \end{pmatrix} + \frac{2t^2}{\epsilon - U'} \begin{pmatrix} 1 & 1 \\ 1 & 1 \end{pmatrix} \right] v_2 = \epsilon v_2$$

$$\begin{pmatrix} b + U & b \\ b & b + U \end{pmatrix} v_2 = \epsilon v_2 \quad , \; b \equiv \frac{2t^2}{\epsilon - U'}$$

and thus $\epsilon = (b + U') \pm b$ or:

$$\epsilon_{1,2} = \frac{1}{2} \left(U' + U \pm \sqrt{(U' - U)^2 + 16t^2} \right) \qquad \epsilon_4 = U \tag{58}$$

The eigenenergy of the ground state is therefore

$$\epsilon_0 = \epsilon_2 = \frac{1}{2} \left(U' + U - \sqrt{(U' - U)^2 + 16t^2} \right) \tag{59}$$

Next, the ground state's eigenvector is obtained by solving the following equation system:

$$\begin{pmatrix} U' & 0 & t & t \\ 0 & U' & -t & -t \\ t & -t & U & 0 \\ t & -t & 0 & U \end{pmatrix} \begin{pmatrix} a \\ b \\ c \\ d \end{pmatrix} = \epsilon_0 \begin{pmatrix} a \\ b \\ c \\ d \end{pmatrix} \tag{60}$$

The equations yield $a = -b$, $c = d$ and $c = 2tb/(U - \epsilon_2)$. Along with normalization this results in the following eigenvector for ϵ_0:

$$\left| \psi_0^{(2)} \right\rangle = \frac{1}{\sqrt{2}} \frac{1}{\sqrt{(\epsilon_2 - U)^2 + 4t^2}} \begin{pmatrix} \epsilon_2 - U \\ U - \epsilon_2 \\ 2t \\ 2t \end{pmatrix} \tag{61}$$

where (2) indicates two involved particles. For N=1 particles there are the following states:

$$|1\rangle = |\uparrow \cdot\rangle = \hat{c}^\dagger_{1\uparrow} |0\rangle$$
$$|2\rangle = |\downarrow \cdot\rangle = \hat{c}^\dagger_{1\downarrow} |0\rangle$$
$$|3\rangle = |\cdot \uparrow\rangle = \hat{c}^\dagger_{2\uparrow} |0\rangle$$
$$|4\rangle = |\cdot \downarrow\rangle = \hat{c}^\dagger_{2\downarrow} |0\rangle$$

resulting in the following matrix:

$$\begin{pmatrix} 0 & 0 & t & 0 \\ 0 & 0 & 0 & t \\ t & 0 & 0 & 0 \\ 0 & t & 0 & 0 \end{pmatrix} \tag{62}$$

Solving this matrix grants two-fold degenerate eigenvalues and their eigenvectors:

$$\begin{aligned} \left|\psi_1^{(1)}\right\rangle &= \frac{1}{\sqrt{2}}(\hat{c}^\dagger_{1\uparrow} + \hat{c}^\dagger_{2\uparrow})\left|0\right\rangle & \epsilon_1^{(1)} &= t \\ \left|\psi_2^{(1)}\right\rangle &= \frac{1}{\sqrt{2}}(\hat{c}^\dagger_{1\downarrow} + \hat{c}^\dagger_{2\downarrow})\left|0\right\rangle & \epsilon_2^{(1)} &= t \\ \left|\psi_3^{(1)}\right\rangle &= \frac{1}{\sqrt{2}}(\hat{c}^\dagger_{1\uparrow} - \hat{c}^\dagger_{2\uparrow})\left|0\right\rangle & \epsilon_3^{(1)} &= -t \\ \left|\psi_4^{(1)}\right\rangle &= \frac{1}{\sqrt{2}}(\hat{c}^\dagger_{1\downarrow} - \hat{c}^\dagger_{2\downarrow})\left|0\right\rangle & \epsilon_4^{(1)} &= -t \end{aligned}$$

For $N = 3$ the possible states are:

$$\begin{aligned} \left|1\right\rangle &= \left|\uparrow \cdot \uparrow\downarrow\right\rangle = \hat{c}^\dagger_{1\uparrow} c^\dagger_{2\uparrow} c^\dagger_{2\downarrow}\left|0\right\rangle \\ \left|2\right\rangle &= \left|\downarrow \cdot \uparrow\downarrow\right\rangle = \hat{c}^\dagger_{1\downarrow} c^\dagger_{2\uparrow} c^\dagger_{2\downarrow}\left|0\right\rangle \\ \left|3\right\rangle &= \left|\uparrow\downarrow \cdot \uparrow\right\rangle = c^\dagger_{1\uparrow} c^\dagger_{1\downarrow} \hat{c}^\dagger_{2\uparrow}\left|0\right\rangle \\ \left|4\right\rangle &= \left|\uparrow\downarrow \cdot \downarrow\right\rangle = c^\dagger_{1\uparrow} c^\dagger_{1\downarrow} \hat{c}^\dagger_{2\downarrow}\left|0\right\rangle \end{aligned}$$

Resulting in the following matrix

$$\begin{pmatrix} U + 2U' & 0 & -t & 0 \\ 0 & U + 2U' & 0 & -t \\ -t & 0 & U + 2U' & 0 \\ 0 & -t & 0 & U + 2U' \end{pmatrix} \tag{63}$$

Solving the matrix grants the following eigenvalues and -vectors:

$$\begin{aligned} \left|\psi_1^{(3)}\right\rangle &= \frac{1}{\sqrt{2}}(\hat{c}^\dagger_{1\uparrow} c^\dagger_{2\uparrow} c^\dagger_{2\downarrow} + c^\dagger_{1\uparrow} c^\dagger_{1\downarrow} \hat{c}^\dagger_{2\uparrow})\left|0\right\rangle & \epsilon_1^{(3)} &= U + 2U' - t \\ \left|\psi_2^{(3)}\right\rangle &= \frac{1}{\sqrt{2}}(\hat{c}^\dagger_{1\downarrow} c^\dagger_{2\uparrow} c^\dagger_{2\downarrow} + c^\dagger_{1\uparrow} c^\dagger_{1\downarrow} \hat{c}^\dagger_{2\downarrow})\left|0\right\rangle & \epsilon_2^{(3)} &= U + 2U' - t \\ \left|\psi_3^{(3)}\right\rangle &= \frac{1}{\sqrt{2}}(\hat{c}^\dagger_{1\uparrow} c^\dagger_{2\uparrow} c^\dagger_{2\downarrow} - c^\dagger_{1\uparrow} c^\dagger_{1\downarrow} \hat{c}^\dagger_{2\uparrow})\left|0\right\rangle & \epsilon_3^{(3)} &= U + 2U' + t \\ \left|\psi_4^{(3)}\right\rangle &= \frac{1}{\sqrt{2}}(\hat{c}^\dagger_{1\downarrow} c^\dagger_{2\uparrow} c^\dagger_{2\downarrow} - c^\dagger_{1\uparrow} c^\dagger_{1\downarrow} \hat{c}^\dagger_{2\downarrow})\left|0\right\rangle & \epsilon_4^{(3)} &= U + 2U' + t \end{aligned}$$

to sum up the results:

$$\left|\psi_0^{(2)}\right\rangle = \frac{a}{\sqrt{2}}(|\uparrow\cdot\downarrow\rangle - |\downarrow\cdot\uparrow\rangle) + \frac{b}{\sqrt{2}}(|\uparrow\downarrow\cdot\ \rangle + |\ \cdot\uparrow\downarrow\rangle) \quad , \quad \epsilon_0^{(2)} = \frac{1}{2}(U' + U - \sqrt{(U'-U)^2 + 16t^2})$$

$$a = \frac{\epsilon_0^{(2)} - U}{\sqrt{(\epsilon_0^{(2)} - U)^2 + 4t^2}} \qquad , \qquad b = \frac{2t}{\sqrt{(\epsilon_0^{(2)} - U)^2 + 4t^2}}$$

$$\left|\psi_1^{(1)}\right\rangle = \frac{1}{\sqrt{2}}(|\uparrow\cdot\ \rangle + |\ \cdot\uparrow\rangle) \quad , \quad \epsilon_1^{(1)} = t$$

$$\left|\psi_2^{(1)}\right\rangle = \frac{1}{\sqrt{2}}(|\downarrow\cdot\ \rangle + |\ \cdot\downarrow\rangle) \quad , \quad \epsilon_2^{(1)} = t$$

$$\left|\psi_3^{(1)}\right\rangle = \frac{1}{\sqrt{2}}(|\ \cdot\uparrow\rangle - |\uparrow\cdot\ \rangle) \quad , \quad \epsilon_3^{(1)} = -t$$

$$\left|\psi_4^{(1)}\right\rangle = \frac{1}{\sqrt{2}}(|\ \cdot\downarrow\rangle - |\downarrow\cdot\ \rangle) \quad , \quad \epsilon_4^{(1)} = -t$$

$$\left|\psi_1^{(3)}\right\rangle = \frac{1}{\sqrt{2}}(|\uparrow\cdot\uparrow\downarrow\rangle + |\uparrow\downarrow\cdot\uparrow\rangle) \quad , \quad \epsilon_1^{(3)} = U + 2U' - t$$

$$\left|\psi_2^{(3)}\right\rangle = \frac{1}{\sqrt{2}}(|\downarrow\cdot\uparrow\downarrow\rangle + |\uparrow\downarrow\cdot\downarrow\rangle) \quad , \quad \epsilon_2^{(3)} = U + 2U' - t$$

$$\left|\psi_3^{(3)}\right\rangle = \frac{1}{\sqrt{2}}(|\uparrow\cdot\uparrow\downarrow\rangle - |\uparrow\downarrow\cdot\uparrow\rangle) \quad , \quad \epsilon_3^{(3)} = U + 2U' + t$$

$$\left|\psi_4^{(3)}\right\rangle = \frac{1}{\sqrt{2}}(|\downarrow\cdot\uparrow\downarrow\rangle - |\uparrow\downarrow\cdot\downarrow\rangle) \quad , \quad \epsilon_4^{(3)} = U + 2U' + t$$

Now the Green's function can be calculated by using the Lehmann representation from Eq. (8) in matrix form:

$$G_{ij,\sigma\sigma'}(\omega) = \sum_n \left[\frac{\left\langle \psi_0^{(N)} \right| c_{i\sigma} \left| \psi_n^{(N+1)} \right\rangle \left\langle \psi_n^{(N+1)} \right| c_{j\sigma'}^{\dagger} \left| \psi_0^{(N)} \right\rangle}{\omega - \epsilon_n^{(N+1)} + \epsilon_0^{(N)} + i\delta} + \frac{\left\langle \psi_0^{(N)} \right| c_{j\sigma'}^{\dagger} \left| \psi_n^{(N-1)} \right\rangle \left\langle \psi_n^{(N-1)} \right| c_{i\sigma} \left| \psi_0^{(N)} \right\rangle}{\omega + \epsilon_n^{(N-1)} - \epsilon_0^{(N)} - i\delta} \right] \tag{64}$$

The products of the first term yield

$$\left\langle \psi_0^{(2)} \right| c_{i\sigma} \left| \psi_1^{(3)} \right\rangle = \frac{1}{2}(-a\delta_{i2}\delta_{\sigma\uparrow} + b\delta_{i1}\delta_{\sigma\uparrow} - a\delta_{i1}\delta_{\sigma\uparrow} + b\delta_{i2}\delta_{\sigma\uparrow}) = \frac{1}{2}(b-a)\delta_{\sigma\uparrow}$$

$$\left\langle \psi_0^{(2)} \right| c_{i\sigma} \left| \psi_2^{(3)} \right\rangle = \frac{1}{2}(-a\delta_{i2}\delta_{\sigma\downarrow} + b\delta_{i1}\delta_{\sigma\downarrow} - a\delta_{i1}\delta_{\sigma\downarrow} + b\delta_{i2}\delta_{\sigma\downarrow}) = \frac{1}{2}(b-a)\delta_{\sigma\downarrow}$$

$$\left\langle \psi_0^{(2)} \right| c_{i\sigma} \left| \psi_3^{(3)} \right\rangle = \frac{1}{2}(-a\delta_{i2}\delta_{\sigma\uparrow} + b\delta_{i1}\delta_{\sigma\uparrow} + a\delta_{i1}\delta_{\sigma\uparrow} - b\delta_{i2}\delta_{\sigma\uparrow}) = -\frac{(-1)^i}{2}(b+a)\delta_{\sigma\uparrow}$$

$$\left\langle \psi_0^{(2)} \right| c_{i\sigma} \left| \psi_4^{(3)} \right\rangle = \frac{1}{2}(-a\delta_{i2}\delta_{\sigma\downarrow} + b\delta_{i1}\delta_{\sigma\downarrow} + a\delta_{i1}\delta_{\sigma\downarrow} - b\delta_{i2}\delta_{\sigma\downarrow}) = -\frac{(-1)^i}{2}(b+a)\delta_{\sigma\downarrow}$$

Thus the first term is

$$\begin{aligned}
G^{(3)}_{ij,\sigma\sigma'}(\omega) &= \frac{(\frac{b-a}{2})^2\delta_{\sigma\uparrow}\delta_{\sigma'\uparrow}}{\omega-(U+2U'-t)+\epsilon_0+i\delta} + \frac{(\frac{b-a}{2})^2\delta_{\sigma\downarrow}\delta_{\sigma'\downarrow}}{\omega-(U+2U'-t)+\epsilon_0+i\delta} \\
&+ \frac{(-1)^{i+j}(\frac{b+a}{2})^2\delta_{\sigma\uparrow}\delta_{\sigma'\uparrow}}{\omega-(U+2U'+t)+\epsilon_0+i\delta} + \frac{(-1)^{i+j}(\frac{b+a}{2})^2\delta_{\sigma\downarrow}\delta_{\sigma'\downarrow}}{\omega-(U+2U'+t)+\epsilon_0+i\delta} \\
\\
&= \frac{(\frac{b-a}{2})^2\delta_{\sigma\sigma'}}{\omega-(U+2U'-t)+\epsilon_0+i\delta} + \frac{(-1)^{i+j}(\frac{b+a}{2})^2\delta_{\sigma\sigma'}}{\omega-(U+2U'+t)+\epsilon_0+i\delta}
\end{aligned}$$

Analogous for the second term the products are

$$\begin{aligned}
\left\langle \psi_0^{(2)} \right| c^\dagger_{i\sigma} \left| \psi_1^{(1)} \right\rangle &= \frac{1}{2}(-a\delta_{i2}\delta_{\sigma\downarrow} - b\delta_{i1}\delta_{\sigma\downarrow} - a\delta_{i1}\delta_{\sigma\downarrow} - b\delta_{i2}\delta_{\sigma\downarrow}) = -\frac{1}{2}(b+a)\delta_{\sigma\downarrow} \\
\left\langle \psi_0^{(2)} \right| c^\dagger_{i\sigma} \left| \psi_2^{(1)} \right\rangle &= \frac{1}{2}(+a\delta_{i2}\delta_{\sigma\uparrow} + b\delta_{i1}\delta_{\sigma\uparrow} + a\delta_{i1}\delta_{\sigma\uparrow} + b\delta_{i2}\delta_{\sigma\uparrow}) = +\frac{1}{2}(b+a)\delta_{\sigma\uparrow} \\
\left\langle \psi_0^{(2)} \right| c^\dagger_{i\sigma} \left| \psi_3^{(1)} \right\rangle &= \frac{1}{2}(+a\delta_{i2}\delta_{\sigma\downarrow} + b\delta_{i1}\delta_{\sigma\downarrow} - a\delta_{i1}\delta_{\sigma\downarrow} - b\delta_{i2}\delta_{\sigma\downarrow}) = -\frac{(-1)^i}{2}(b-a)\delta_{\sigma\downarrow} \\
\left\langle \psi_0^{(2)} \right| c^\dagger_{i\sigma} \left| \psi_4^{(1)} \right\rangle &= \frac{1}{2}(-a\delta_{i2}\delta_{\sigma\uparrow} - b\delta_{i1}\delta_{\sigma\uparrow} + a\delta_{i1}\delta_{\sigma\uparrow} + b\delta_{i2}\delta_{\sigma\uparrow}) = +\frac{(-1)^i}{2}(b-a)\delta_{\sigma\uparrow}
\end{aligned}$$

resulting in

$$\begin{aligned}
G^{(1)}_{ij,\sigma\sigma'}(\omega) &= \frac{(\frac{b+a}{2})^2\delta_{\sigma\downarrow}\delta_{\sigma'\downarrow}}{\omega+t-\epsilon_0-i\delta} + \frac{(\frac{b+a}{2})^2\delta_{\sigma\uparrow}\delta_{\sigma'\uparrow}}{\omega+t-\epsilon_0-i\delta} \\
&+ \frac{(-1)^{i+j}(\frac{b-a}{2})^2\delta_{\sigma\uparrow}\delta_{\sigma'\uparrow}}{\omega-t-\epsilon_0-i\delta} + \frac{(-1)^{i+j}(\frac{b-a}{2})^2\delta_{\sigma\downarrow}\delta_{\sigma'\downarrow}}{\omega-t-\epsilon_0-i\delta} \\
\\
&= \frac{(\frac{b+a}{2})^2\delta_{\sigma\sigma'}}{\omega+t-\epsilon_0-i\delta} + \frac{(-1)^{i+j}(\frac{b-a}{2})^2\delta_{\sigma\sigma'}}{\omega-t-\epsilon_0-i\delta}
\end{aligned}$$

Summed together, the exact Green function is gained:

$$\begin{aligned}
G^{(2)}_{ij,\sigma}(\omega) &= \frac{(\frac{b+a}{2})^2}{\omega+t-\epsilon_0-i\delta} + \frac{(-1)^{i+j}(\frac{b-a}{2})^2}{\omega-t-\epsilon_0-i\delta} \\
&+ \frac{(\frac{b-a}{2})^2}{\omega-(U+2U'-t)+\epsilon_0+i\delta} + \frac{(-1)^{i+j}(\frac{b+a}{2})^2}{\omega-(U+2U'+t)+\epsilon_0+i\delta}
\end{aligned}$$

$$\begin{aligned}
\epsilon_0^{(2)} &= \frac{1}{2}(U'+U-\sqrt{(U'-U)^2+16t^2}) \\
a &= \frac{\epsilon_0^{(2)}-U}{\sqrt{(\epsilon_0^{(2)}-U)^2+4t^2}} \quad , \quad b = \frac{2t}{\sqrt{(\epsilon_0^{(2)}-U)^2+4t^2}}
\end{aligned}$$

For the non-interacting case U and U' are set to zero, resulting in $\epsilon_0 = -2|t|$, $a = -1/\sqrt{2}$ and $b = sgn(t)/\sqrt{2}$ and thus for $t > 0$:

$$G^0_{ij,\sigma}(\omega) = \frac{1}{2}\left(\frac{(-1)^{i+j}}{\omega+t-i\delta} + \frac{1}{\omega-t+i\delta}\right) \tag{65}$$

8.2 The atomic problem - solved with GW

This section treats the analytic calculation of the GWA on the atomic model. Analogous to the GWA application to the crystal model, only one-shot will be conducted, starting with the determination of the non-interacting polarization P^0. According to the Hedin equations the polarization is

$$P_{ij}(\omega) = -\frac{i}{2\pi}\sum_{\sigma}\int_{-\infty}^{+\infty} d\omega' G_{ij,\sigma}(\omega'+\omega)G_{ji,\sigma}(\omega') \tag{66}$$

Inserting G^0 from Appx. (8.1) results in

$$\begin{aligned}
P^0_{ij}(\omega) &= -\frac{i}{2\pi}\underbrace{2}_{spin}\int_{-\infty}^{+\infty} d\omega' \left(\frac{(-1)^{i+j}\frac{1}{2}}{\omega'+\omega+t-i\delta}+\frac{\frac{1}{2}}{\omega'+\omega-t+i\delta}\right)\left(\frac{(-1)^{i+j}\frac{1}{2}}{\omega'+t-i\delta}+\frac{\frac{1}{2}}{\omega'-t+i\delta}\right)\\
&= -\frac{i}{4\pi}\int_{-\infty}^{+\infty} d\omega' \left(\frac{1}{\omega'+\omega+t-i\delta}\frac{1}{\omega'+t-i\delta}+\frac{(-1)^{i+j}}{\omega'+\omega+t-i\delta}\frac{1}{\omega'-t+i\delta}+\right.\\
&\qquad\left.+\frac{1}{\omega'+\omega-t+i\delta}\frac{(-1)^{i+j}}{\omega'+t-i\delta}+\frac{1}{\omega'+\omega-t+i\delta}\frac{1}{\omega'-t+i\delta}\right)
\end{aligned}$$

Doing a contour integral in the upper domain yields zero for the first and last terms so that only the second and third integral terms are left, which lets the polarization become

$$P^0_{ij}(\omega) = -\frac{i}{4\pi}\left(\frac{-2\pi i}{\omega+2t-i\delta}+\frac{2\pi i}{\omega-2t+i\delta}\right)(-1)^{i+j} = \frac{(-1)^{i+j}}{2}\left(\frac{1}{\omega-2t+i\delta}-\frac{1}{\omega+2t-i\delta}\right)$$

Introducing the Coulomb interaction matrix,

$$U_{ij} = U\delta_{ij}+U'(1-\delta_{ij}) = \begin{pmatrix} U & U' \\ U' & U \end{pmatrix} \tag{67}$$

the screened Coulomb interaction is determined next:

$$\begin{aligned}
W(1,2) &= v(1-2)+\int d3d4v(1-3)P^0(3,4)W(4,2)\\
W_{ij}(\omega) &= U_{ij}+\sum_{kl}U_{ik}P^0_{kl}(\omega)W_{lj}(\omega)\\
U_{ij} &= W_{ij}(\omega)-\sum_{kl}U_{ik}P^0_{kl}(\omega)W_{lj}(\omega)\\
U_{ij} &= \sum_{kl}\delta_{li}\delta_{kl}W_{lj}(\omega)-\sum_{kl}U_{ik}P^0_{kl}(\omega)W_{lj}(\omega)\\
U_{ij} &= \sum_{kl}(\delta_{li}\delta_{kl}-U_{ik}P^0_{kl}(\omega))W_{lj}(\omega)\\
U_{ij} &= \sum_{l}\epsilon_{il}(\omega)W_{lj}(\omega)\\
\Leftrightarrow W_{ij} &= \sum_{l}\epsilon_{il}(\omega)^{-1}U_{lj}(\omega)
\end{aligned}$$

Where the dielectric function was introduced:

$$\begin{aligned}
\epsilon_{il}(\omega) &= \sum_k (\delta_{li}\delta_{kl} - U_{ik}P^0_{kl}(\omega)) = \delta_{li} - \sum_k U_{ik}P^0_{kl}(\omega) \\
&= \delta_{li} - \sum_k U_{ik}\frac{(-1)^{k+l}}{2}\left(\frac{1}{\omega - 2t + i\delta} - \frac{1}{\omega + 2t - i\delta}\right) \\
&= \delta_{li} - \sum_k U_{ik}\frac{(-1)^{k+l}}{2}\left(\frac{4t - 2i\delta}{(\omega - 2t + i\delta)(\omega + 2t - i\delta)}\right) \\
&= \delta_{li} + (-1)^l (U_{i1} - U_{i2})\frac{2t - i\delta}{(\omega - 2t + i\delta)(\omega + 2t - i\delta)} \\
&\equiv \delta_{li} + (-1)^l (U_{i1} - U_{i2})\frac{2t - i\delta}{A(\omega)} \\
&= \left[1 - (U - U')\frac{2t - i\delta}{A(\omega)}\right]\delta_{il} + \left[(U - U')\frac{2t - i\delta}{A(\omega)}\right](1 - \delta_{il}) \\
&\equiv \left(1 + \frac{a}{A(\omega)}\right)\delta_{il} + \left(\frac{-a}{A(\omega)}\right)(1 - \delta_{il}) \\
&\text{with} \quad a = (U - U')(-2t + i\delta)
\end{aligned}$$

By using Cramer's rule, the inverse can be calculated:

$$\begin{aligned}
(\epsilon^{-1})_{ij} &= \frac{(-1)^{i+j} \cdot e_{ji}}{det(\epsilon)} \qquad \text{, where } e_{ij} \text{ are minors of } \epsilon \\
\det(\epsilon(\omega)) &= \left(1 + \frac{a}{A(\omega)}\right)^2 - \left(\frac{-a}{A(\omega)}\right)^2 = 1 + \frac{2a}{A(\omega)} \\
e_{11} &= \epsilon_{22} = \epsilon_{11} = e_{22} \\
e_{21} &= \epsilon_{12} = \epsilon_{21} = e_{21} \\
(\epsilon^{-1})_{ij} &= \frac{\left(1 + \frac{a}{A(\omega)}\right)\delta_{ij} - \left(\frac{-a}{A(\omega)}\right)(1 - \delta_{ij})}{1 + \frac{2a}{A(\omega)}} \\
&= \frac{(A(\omega) + a)\,\delta_{ij} + a(1 - \delta_{ij})}{A(\omega) + 2a}
\end{aligned}$$

Thus the screened interaction becomes

$$\begin{aligned}
W_{ij}(\omega) &= \sum_l \epsilon_{il}(\omega)^{-1}U_{lj}(\omega) = \sum_l \left(\frac{(A(\omega) + a)\,\delta_{il} + a(1 - \delta_{il})}{A(\omega) + 2a}\right)U_{lj} \\
&= \left(\frac{(A(\omega) + a)\,\delta_{i1} + a(1 - \delta_{i1})}{A(\omega) + 2a}\right)U_{1j} + \left(\frac{(A(\omega) + a)\,\delta_{i2} + a(1 - \delta_{i2})}{A(\omega) + 2a}\right)U_{2j} \\
W_{11}(\omega) &= \left(\frac{A(\omega) + a}{A(\omega) + 2a}\right)U + \left(\frac{a}{A(\omega) + 2a}\right)U' = U - \frac{a(U - U')}{A(\omega) + 2a} = W_{22}(\omega) \\
W_{12}(\omega) &= \left(\frac{A(\omega) + a}{A(\omega) + 2a}\right)U' + \left(\frac{a}{A(\omega) + 2a}\right)U = U' + \frac{a(U - U')}{A(\omega) + 2a} = W_{21}(\omega)
\end{aligned}$$

Expanding $A(\omega)$:

$$\begin{aligned}
A(\omega) + 2a &= (\omega - 2t + i\delta)(\omega + 2t - i\delta) + (U - U')(-2t + i\delta) \\
&= \omega^2 - \underbrace{4(t^2 + (U - U')t)}_{x} + \underbrace{(4t + 2(U - U'))}_{y} \cdot i\delta \\
&= \omega^2 - (\sqrt{x - y \cdot i\delta})^2 = (\omega - \sqrt{x - y \cdot i\delta})(\omega + \sqrt{x - y \cdot i\delta}) \\
&\text{Taylor expand the square root around } \delta \to 0\text{:} \\
&\approx (\omega - \sqrt{x} + \frac{y}{\sqrt{x}} \cdot i\delta)(\omega + \sqrt{x} - \frac{y}{\sqrt{x}} \cdot i\delta) \\
&\equiv (\omega + b)(\omega - b)
\end{aligned}$$

To sum up:

$$\begin{aligned}
\frac{1}{(\omega + b)(\omega - b)} &= \frac{1}{2b} \frac{(\omega + b) - (\omega - b)}{(\omega + b)(\omega - b)} \\
&= \frac{1}{2b} \left(\frac{1}{\omega - b} - \frac{1}{\omega + b} \right)
\end{aligned}$$

$$\begin{aligned}
W^0_{ij}(\omega) &= U_{ij} - (-1)^{i+j} \frac{a'}{2b} \left(\frac{1}{\omega - b} - \frac{1}{\omega + b} \right) \\
&\quad \text{with } a' = a(U - U') = (U - U')^2(-2t + i\delta) \\
G^0_{ij}(\omega) &= \frac{1}{2} \left(\frac{(-1)^{i+j}}{\omega + t - i\delta} + \frac{1}{\omega - t + i\delta} \right) \\
&\equiv \frac{1}{2} \left(\frac{(-1)^{i+j}}{\omega - c} + \frac{1}{\omega + c} \right)
\end{aligned}$$

Now the self energy can be determined via the GW approximation:

$$\Sigma^{GW}_{ij,\sigma}(\omega) = i \int \frac{d\omega'}{2\pi} G_{ij,\sigma}(\omega + \omega') W_{ji}(\omega') \tag{68}$$

After plugging in G^0 and W^0:

$$\begin{aligned}
\Sigma_{ij}(\omega) &= \frac{i}{2\pi} \int d\omega' \left(\frac{1}{2} \left(\frac{(-1)^{i+j}}{\omega + \omega' - c} + \frac{1}{\omega + \omega' + c} \right) \right) \left(U_{ij} - (-1)^{i+j} \frac{a'}{2b} \left(\frac{1}{\omega - b} - \frac{1}{\omega + b} \right) \right) \\
&= \frac{i}{4\pi} \int d\omega' \left(\frac{(-1)^{i+j} U_{ij}}{\omega' + \omega - c} - \frac{a'}{2b(\omega' + \omega - c)(\omega' - b)} + \frac{a'}{2b(\omega' + \omega - c)(\omega' + b)} \right. \\
&\qquad \left. + \frac{U_{ij}}{\omega' + \omega + c} - \frac{(-1)^{i+j} a'}{2b(\omega' + \omega + c)(\omega' - b)} + \frac{a'}{2b(\omega' + \omega + c)(\omega' + b)} \right)
\end{aligned}$$

Calculating the 6 contour integrals by closing the contour in the upper domain:

$$\int d\omega' \frac{1}{\omega' + \omega - c} = 2\pi i$$

$$\begin{aligned}
\int d\omega' \frac{1}{(\omega' + \omega - c)(\omega' - b)} &= \left.\frac{2\pi i}{(\omega' - b)}\right|_{\omega' = c-\omega} + \left.\frac{2\pi i}{(\omega' + \omega - c)}\right|_{\omega' = b} \\
&= -\frac{2\pi i}{\omega + b - c} + \frac{2\pi i}{\omega + b - c} = 0 \\
\int d\omega' \frac{1}{(\omega' + \omega - c)(\omega' + b)} &= \left.\frac{2\pi i}{(\omega' + b)}\right|_{\omega' = c-\omega} = -\frac{2\pi i}{\omega - b - c}
\end{aligned}$$

$$\int d\omega' \frac{1}{\omega' + \omega + c} = 0$$

$$\begin{aligned}
\int d\omega' \frac{1}{(\omega' + \omega + c)(\omega' - b)} &= \left.\frac{2\pi i}{(\omega' + \omega + c)}\right|_{\omega' = b} = \frac{2\pi i}{\omega + b + c} \\
\int d\omega' \frac{1}{(\omega' + \omega + c)(\omega' + b)} &= \left.\frac{2\pi i}{(\omega' + b)}\right|_{\omega' = -\omega-c} + \left.\frac{2\pi i}{(\omega' + \omega + c)}\right|_{\omega' = -b} \\
&= -\frac{2\pi i}{\omega - b + c} + \frac{2\pi i}{\omega - b + c} = 0
\end{aligned}$$

Thus, the analytic self-energy in the one-shot GW approximation becomes

$$\begin{aligned}
\Sigma_{ij}(\omega) &= \frac{i}{4\pi}\left(2\pi i(-1)^{i+j}U_{ij} - \frac{a'}{2b}\frac{2\pi i}{\omega - b - c} - \frac{(-1)^{i+j}a'}{2b}\frac{2\pi i}{\omega + b + c}\right) \\
&= -(-1)^{i+j}\frac{U_{ij}}{2} + \frac{a'}{4b}\left(\frac{1}{\omega - b - c} + \frac{(-1)^{i+j}}{\omega + b + c}\right)
\end{aligned}$$

with

$$\begin{aligned}
a' &= (U - U')^2(-2t + i\delta) \\
b &= -\sqrt{4t^2 + 4(U - U')t - (4t + 2(U - U'))\cdot i\delta} \rightarrow -\sqrt{4t^2 + 4(U - U')t} + i\delta \\
c &= -t + i\delta
\end{aligned}$$

8.3 Orbital and band basis

Switching an observable between the orbital basis (1,2) and the band basis (bonding, anti-bonding)

$$\phi_B = \frac{1}{\sqrt{2}}(\phi_1 + \phi_2) \qquad\qquad \phi_A = \frac{1}{\sqrt{2}}(\phi_1 - \phi_2) \tag{69}$$

$$\begin{aligned}
\langle\phi_B|\,\Sigma\,|\phi_B\rangle &= \frac{1}{2}\,\langle\phi_1 + \phi_2|\,\Sigma\,|\phi_1 + \phi_2\rangle \\
&= \frac{1}{2}(\Sigma_{11} + \Sigma_{12} + \Sigma_{21} + \Sigma_{22}) \\
symmetry &= \Sigma_{11} + \Sigma_{12}
\end{aligned}$$

$$\begin{aligned}
\langle\phi_A|\,\Sigma\,|\phi_A\rangle &= \frac{1}{2}\,\langle\phi_1 - \phi_2|\,\Sigma\,|\phi_1 - \phi_2\rangle \\
&= \frac{1}{2}(\Sigma_{11} - \Sigma_{12} - \Sigma_{21} + \Sigma_{22}) \\
symmetry &= \Sigma_{11} - \Sigma_{12}
\end{aligned}$$

$$\begin{aligned}
\langle\phi_B|\,\Sigma\,|\phi_A\rangle &= \frac{1}{2}\,\langle\phi_1 + \phi_2|\,\Sigma\,|\phi_1 - \phi_2\rangle \\
&= \frac{1}{2}(\Sigma_{11} - \Sigma_{12} + \Sigma_{21} - \Sigma_{22}) \\
symmetry &= 0
\end{aligned}$$

References

[1] Vladimir I. Anisimov. *Strong Coulomb Correlations in Electronic Structure Calculations*. Google-Books-ID: 3sjJkC8yN8QC. CRC Press, May 30, 2000. 340 pp. ISBN: 978-90-5699-131-9.

[2] F. Aryasetiawan, L. Hedin, and K. Karlsson. "Multiple Plasmon Satellites in Na and Al Spectral Functions from Ab Initio Cumulant Expansion". In: *Physical Review Letters* 77.11 (Sept. 9, 1996), pp. 2268–2271. DOI: `10.1103/PhysRevLett.77.2268`. URL: `https://link.aps.org/doi/10.1103/PhysRevLett.77.2268`.

[3] Lewin Boehnke et al. "When strong correlations become weak: Consistent merging of GW and DMFT". In: *Physical Review B* 94.20 (Nov. 10, 2016), p. 201106. ISSN: 2469-9950, 2469-9969. DOI: `10.1103/PhysRevB.94.201106`. arXiv: `1604.02023`. URL: `http://arxiv.org/abs/1604.02023`.

[4] *Bonding and antibonding orbitals*. Chemistry LibreTexts. Oct. 2, 2013. URL: `https://chem.libretexts.org/Bookshelves/Physical_and_Theoretical_Chemistry_Textbook_Maps/Supplemental_Modules_(Physical_and_Theoretical_Chemistry)/Chemical_Bonding/Molecular_Orbital_Theory/Bonding_and_antibonding_orbitals` (visited on 07/01/2019).

[5] Henry Ehrenreich, Frederick Seitz, and David Turnbull. *Solid state physics: advances in research and applications. Volume 23 Chapter I*. OCLC: 646775711. New York: Academic Press, 1969. ISBN: 978-0-08-086487-7 978-0-12-607723-0. URL: `http://public.eblib.com/choice/publicfullrecord.aspx?p=405330`.

[6] Matteo Gatti. "The one-particle Green's function and the GW approximation". URL: `http://benasque.org/2012tddft/talks_contr/049_12benasque_gw.pdf` (visited on 02/28/2019).

[7] Florian Gebhard. *The Mott Metal-Insulator Transition: Models and Methods*. Google-Books-ID: HyzyBwAAQBAJ. Springer, July 1, 2003. 338 pp. ISBN: 978-3-540-14858-6.

[8] Lars Hedin. "New Method for Calculating the One-Particle Green's Function with Application to the Electron-Gas Problem". In: *Physical Review* 139.3 (Aug. 2, 1965), A796–A823. DOI: `10.1103/PhysRev.139.A796`. URL: `https://link.aps.org/doi/10.1103/PhysRev.139.A796`.

[9] P. Hohenberg and W. Kohn. "Inhomogeneous Electron Gas". In: *Physical Review* 136.3 (Nov. 9, 1964), B864–B871. DOI: `10.1103/PhysRev.136.B864`. URL: `https://link.aps.org/doi/10.1103/PhysRev.136.B864`.

[10] Hubbard J. and Flowers Brian Hilton. "Electron correlations in narrow energy bands". In: *Proceedings of the Royal Society of London. Series A. Mathematical and Physical Sciences* 276.1365 (Nov. 26, 1963), pp. 238–257. DOI: `10.1098/rspa.1963.0204`. URL: `https://royalsocietypublishing.org/doi/abs/10.1098/rspa.1963.0204`.

[11] Hubbard J. and Flowers Brian Hilton. "Electron correlations in narrow energy bands III. An improved solution". In: *Proceedings of the Royal Society of London. Series A. Mathematical and Physical Sciences* 281.1386 (Sept. 22, 1964), pp. 401–419. DOI: `10.1098/rspa.1964.0190`. URL: `https://royalsocietypublishing.org/doi/abs/10.1098/rspa.1964.0190`.

[12] Masatoshi Imada, Atsushi Fujimori, and Yoshinori Tokura. “Metal-insulator transitions”. In: *Reviews of Modern Physics* 70.4 (Oct. 1, 1998), pp. 1039–1263. DOI: `10.1103/RevModPhys.70.1039`. URL: `https://link.aps.org/doi/10.1103/RevModPhys.70.1039`.

[13] *LAPACK—Linear Algebra PACKage.* URL: `http://www.netlib.org/lapack/` (visited on 04/22/2019).

[14] Mel Levy, John P. Perdew, and Viraht Sahni. “Exact differential equation for the density and ionization energy of a many-particle system”. In: *Physical Review A* 30.5 (Nov. 1, 1984), pp. 2745–2748. DOI: `10.1103/PhysRevA.30.2745`. URL: `https://link.aps.org/doi/10.1103/PhysRevA.30.2745`.

[15] Elliott H. Lieb and F. Y. Wu. “Absence of Mott Transition in an Exact Solution of the Short-Range, One-Band Model in One Dimension”. In: *Physical Review Letters* 20.25 (June 17, 1968), pp. 1445–1448. DOI: `10.1103/PhysRevLett.20.1445`. URL: `https://link.aps.org/doi/10.1103/PhysRevLett.20.1445`.

[16] Inka Laura Marie Locht. “Cohesive and Spectroscopic properties of the Lanthanides within the Hubbard I Approximation”. 2015. URL: `http://urn.kb.se/resolve?urn=urn:nbn:se:uu:diva-267285`.

[17] Walter Metzner and Dieter Vollhardt. “Correlated Lattice Fermions in d=∞ Dimensions”. In: *Physical Review Letters* 62.3 (Jan. 16, 1989), pp. 324–327. DOI: `10.1103/PhysRevLett.62.324`. URL: `https://link.aps.org/doi/10.1103/PhysRevLett.62.324`.

[18] N. F. Mott. “The Basis of the Electron Theory of Metals, with Special Reference to the Transition Metals”. In: *Proceedings of the Physical Society. Section A* 62.7 (July 1949), pp. 416–422. ISSN: 0370-1298. DOI: `10.1088/0370-1298/62/7/303`. URL: `https://doi.org/10.1088%2F0370-1298%2F62%2F7%2F303`.

[19] Fredrik Nilsson. “Unifying first-principles and model approaches for strongly correlated materials: Interplay between long- and short-range correlations”. PhD thesis. Lund University, Jan. 2019. URL: `http://portal.research.lu.se/portal/en/publications/unifying-firstprinciples-and-model-approaches-for-strongly-correlated-materials(2da3bc47-db18-40f0-96c4-9c6b7288a345)/export.html`.

[20] Fredrik Nilsson et al. “Multitier self-consistent GW+EDMFT”. In: *Physical Review Materials* 1.4 (Sept. 21, 2017), p. 043803. ISSN: 2475-9953. DOI: `10.1103/PhysRevMaterials.1.043803`. arXiv: `1706.06808`. URL: `http://arxiv.org/abs/1706.06808`.

[21] Eva Pavarini et al. *DMFT at 25: Infinite Dimensions.* Modeling and Simulation 4. Jülich: Forschungszentrum Jülich Zentralbibliothek, Verlag, 2014. 450 pp. ISBN: 978-3-89336-953-9.

[22] M. J. Rozenberg, X. Y. Zhang, and G. Kotliar. “Mott-Hubbard transition in infinite dimensions”. In: *Physical Review Letters* 69.8 (Aug. 24, 1992), pp. 1236–1239. DOI: `10.1103/PhysRevLett.69.1236`. URL: `https://link.aps.org/doi/10.1103/PhysRevLett.69.1236`.

[23] D. J. Scalapino. “Numerical Studies of the 2D Hubbard Model”. In: *eprint arXiv:cond-mat/0610710* (Oct. 1, 2006), arXiv:cond–mat/0610710. URL: `http://adsabs.harvard.edu/abs/2006cond.mat.10710S`.

[24] M. van Schilfgaarde, T. Kotani, and S. Faleev. “Quasiparticle Self-Consistent GW Theory”. In: *Physical Review Letters* 96.22 (June 6, 2006), p. 226402. ISSN: 0031-9007, 1079-7114. DOI: 10.1103/PhysRevLett.96.226402. arXiv: cond-mat/0510408. URL: http://arxiv.org/abs/cond-mat/0510408.

[25] G. Stefanucci et al. “Diagrammatic expansion for positive spectral functions beyond GW: Application to vertex corrections in the electron gas”. In: *Physical Review B* 90.11 (Sept. 22, 2014), p. 115134. ISSN: 1098-0121, 1550-235X. DOI: 10.1103/PhysRevB.90.115134. arXiv: 1408.6163. URL: http://arxiv.org/abs/1408.6163.

[26] A.-M. S. Tremblay. “Strongly correlated superconductivity”. In: *arXiv:1310.1481 [cond-mat]* (Oct. 5, 2013). arXiv: 1310.1481. URL: http://arxiv.org/abs/1310.1481.

[27] B. Velický, S. Kirkpatrick, and H. Ehrenreich. “Single-Site Approximations in the Electronic Theory of Simple Binary Alloys”. In: *Physical Review* 175.3 (Nov. 15, 1968), pp. 747–766. DOI: 10.1103/PhysRev.175.747. URL: https://link.aps.org/doi/10.1103/PhysRev.175.747.

[28] D. Vollhardt, K. Byczuk, and M. Kollar. “Dynamical Mean-Field Theory”. In: *arXiv:1109.4833 [cond-mat]* 171 (2012), pp. 203–236. DOI: 10.1007/978-3-642-21831-6_7. arXiv: 1109.4833. URL: http://arxiv.org/abs/1109.4833.

[29] Xiaoguang Li Yukuai Liu Yuewei Yin. “Colossal Magnetoresistance Manganites and Related Prototype Devices”. In: *arXiv:1310.1481 [cond-mat]* (Sept. 14, 2013). arXiv: 1309.3681. URL: https://arxiv.org/abs/1309.3681.